Chapter 13
Radiation of Vibrating Structures

Antoine Chaigne

Abstract This chapter deals with the radiation of vibrating structures in air, with application to stringed and percussive instruments. Basic notions are first presented with the help of an introductory example of a beam coupled to an air column. The important concept of critical frequency is then introduced through the example of an infinite thin plate radiating in air. The radiation models of finite plates and their results can be applied to real musical instruments. Recent methods are then presented for calculating the radiation of unbaffled plates, structural volumes, and nonplanar sources. Finally, the questions relative to the appropriate choice of material, and to the compromise between radiation efficiency and tone duration, are illustrated on several stringed instruments.

13.1 Introduction

For a number of musical instruments, the sound results from the vibration of structures. This is the case, for example, for stringed and percussive instruments. Structural acoustics (or *vibroacoustics*) is that subdomain of acoustics dealing with the interaction phenomena between a vibrating structure and the sound field in the adjacent fluid. In what follows, the air is the considered *light* fluid interacting with the structures. The concept of *light* and *heavy* fluid will be defined more formally in this chapter.

The structures used in the making of instrument are most often *thin* structures, which means that their thickness is small compared to the other dimensions. Different types of elastic waves can propagate in these structures. Among them, the flexural waves are those which show the lowest characteristic mechanical impedance. As a consequence, these waves also are those which are the most excited by an impact, and/or by the vibrations of strings coupled to them. The normal velocity and, in turn, the acoustic pressure field, are directly linked to the mechanical vibratory field of the structure.

A. Chaigne (✉)
Institute of Music Acoustics, University of Music and Performing Arts Vienna (MDW), Anton-von-Webern-Platz 1, 1030 Vienna, Austria
e-mail: antchaigne@gmail.com

A. Chaigne, J. Kergomard, *Acoustics of Musical Instruments*, Modern Acoustics and Signal Processing, DOI 10.1007/978-1-4939-3679-3_13

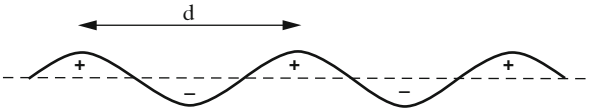

Fig. 13.1 Transverse vibrations of a plate at a frequency close to one on its eigenmodes

In musical acoustics, the most common vibrating structures are plates (guitar, harp, piano soundboards, etc.) or shells (soundboards of bowed strings instruments, bells, gongs, cymbals, etc.). The beams (xylophone, vibraphone, marimba, glockenspiel, etc.) can be considered as limiting cases of plates whose width is small compared to the length. The particular case of the membranes (timpani, drums, etc.) will be treated in detail in Chap. 14.

In contrast with the case of the plane piston seen in Chap. 12, where the surface velocity field is uniform, the vibrations of shells and plates are characterized by the juxtaposition of zones with velocity fields of alternate signs, which can be seen as the 2-D association of dipoles (pairs of monopoles of opposite signs) (see Fig. 13.1). The main effect of this situation is to globally reduce the compression of the fluid (compared to the plane piston), and thus to limit the efficiency of the radiation to the far field. Intuitively, one can feel that the dipoles will produce destructive interferences if $kd \ll 1$, where k is the wavenumber and d the distance between two consecutive "monopoles" on the plate or on the shell. Conversely, if $kd \gg 1$, the monopoles radiate more independently and the radiation efficiency is improved (see also Chap. 12).

As seen in Chap. 3, flexural waves are dispersive, where the phase and group velocities vary with frequency. It will be shown in Sect. 13.3 that the so-called *critical (or coincidence) frequency* f_c exists, for which the acoustic wavelength in the fluid is equal to the elastic wavelength in the structure. For the frequencies smaller than f_c, the sound power radiated by an infinite flat plate is zero, and is very weak for a finite plate. For the shells, and, more generally, for complex structures (such as ribbed plates, for example), the radiation properties depend on the elastic dispersion curve. The phase velocity increases by imposing a curvature to a flat plate: as a consequence, shells are generally more efficient in terms of radiation than plates of similar external surface and thickness, and made of the same material. However, this general tendency needs to be clarified for each particular geometry: in Sect. 13.5, it will be seen on a simple example that the curvature also affects the bandwidth and the directivity of the source.

13.2 Basic Concepts in Structural Acoustics

This chapter starts with the presentation of a simple 1-D example whose aim is to introduce the basic concepts in structural–acoustic coupling. The purpose is to highlight the following properties:

- Both the real and imaginary parts of the eigenfrequencies are modified by the acoustic radiation of a structure. In this section, a method is shown for calculating these modifications. In addition, approximations are presented which are justified in case of weak coupling between the structure and the fluid, as it is often the case for the air.
- Expanding the general solution of a coupled system in terms of the structural in vacuo modes shows that intermodal coupling results from the radiation. In practice, this means that if one particular mode is excited then, in turn, other coupled modes are excited. These phenomena are currently observed in stringed instruments. For a formal point of view, this coupling is indicated through the fact that the differential equations that govern the generalized displacements are not independent from each other anymore. These properties are analogous to those demonstrated in Chap. 5 for the nonproportional damping.[1]
- For a forced excitation at a given frequency ω, it is generally not possible to excite only one mode, as a consequence of the intermodal coupling. Thus, the concept of *Operating Deflexion Shape* (or ODS) needs to be introduced.
- The structural and radiation resistance matrices are introduced by means of an energy analysis of the coupled system. The radiation efficiency is derived from these definitions.

13.2.1 Vibrating Beam Coupled to an Infinite Fluid Medium: Modal Approach

A typical situation involving a vibrating structure radiating sound energy in free space is analyzed here. The simple selected system is composed of a finite elastic beam vibrating longitudinally and loaded at one end by a semi-infinite tube filled with air. This problem shows some analogies with the example of the string with dissipative end studied in Chap. 5.

The system shown in Fig. 13.2 is considered. It is composed of an elastic longitudinally vibrating 1-D beam with density ρ_s, section S, length L, and Young's modulus E. $\xi(x,t)$ is the longitudinal displacement of a current point at position x along the bar (with $0 < x < L$). This beam is coupled at one end ($x = L$) with a semi-infinite tube filled with air, and clamped at the other ($x = 0$). The motion of the beam induces a pressure $p(x,t)$ inside the tube. This pressure reacts on the beam at point $x = L$. $c_L = \sqrt{E/\rho_s}$ is the longitudinal wave speed. The coupled system is governed by the equations:

[1] In reality, the modes of the coupled system are complex, and we could think of applying the rigorous theory of complex modes presented in Chap. 5. However, since the air coupling can be most often considered as weak in musical acoustics, the method of projection on the in vacuo modes is preferred here, which corresponds to current practice.

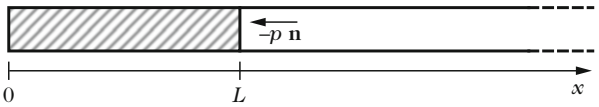

Fig. 13.2 Longitudinally vibrating beam coupled to a semi-infinite tube. In $x = L$, the cross-section of the bar is subjected to the sound pressure $-p\,\boldsymbol{n}$, where $\boldsymbol{n}$ is the unitary vector normal to the beam

$$\begin{cases} \rho_s \frac{\partial^2 \xi}{\partial t^2} = E \frac{\partial^2 \xi}{\partial x^2} \quad \text{for} \quad 0 \le x < L, \\ p(L,t) = \rho c \dot{\xi}(L,t), \\ \xi(0,t) = 0, \\ p(x,t) = \rho c \dot{\xi}(L, t - \frac{x-L}{c}) \quad \text{for} \quad L < x < \infty. \end{cases} \tag{13.1}$$

The system (13.1) is solved by expanding the sought solution $\xi(x,t)$ in terms of the in vacuo modes $\phi_n(x)$ of the beam:

$$\xi(x,t) = \sum_n \phi_n(x) q_n(t), \tag{13.2}$$

where the $q_n(t)$ are the generalized displacements. The system (13.1) is then integrated over the length of the beam (from 0 to L), after multiplication by any eigenfunction ϕ_n. This gives

$$\int_0^L \rho_s S \left(\sum_m \phi_m(x) \ddot{q}_m(t) \right) \phi_n(x)\, dx - \int_0^L ES \left(\sum_m \phi_m''(x) q_m(t) \right) \phi_n(x)\, dx$$
$$= S\rho c \left(\sum_m \phi_m(L) \dot{q}_m(t) \right) \phi_n(L). \tag{13.3}$$

Equation (13.3) expresses the energetic balance between the internal stresses inside the beam, the inertial forces, and the pressure forces applied to the beam by the exterior medium. Due to the orthogonality properties of the in vacuo modes ϕ_n, the only nonzero terms remaining in (13.3) are those for which $m = n$. Introducing further the modal mass:

$$m_n = \int_0^L \rho_s S \phi_n^2(x) dx, \tag{13.4}$$

and rewriting the second integral:

$$-\int_0^L ES \frac{\omega_n^2}{c_L^2} \left(\sum_m \phi_m(x) q_m(t) \right) \phi_n(x)\, dx = -\omega_n^2 m_n q_n(t), \tag{13.5}$$

it is found that the generalized displacements $q_n(t)$ are solutions of the coupled system:

$$m_n\ddot{q}_n(t) + m_n\omega_n^2 q_n(t) = -R_a\phi_n(L)\sum_m \phi_m(L)\dot{q}_m(t), \tag{13.6}$$

where $R_a = \rho cS$ is the radiation resistance. It is observed that one effect of the radiation is to couple together the in vacuo modes of the beam. However, under some restrictive assumptions, it will be allowed to replace the system (13.6) by an approximate uncoupled system.

After determining the generalized displacements q_n, the displacement ξ is derived from (13.2), and this allows to calculate both the velocity and the pressure field. In conclusion, all variables of the problem are known. This justifies to focus primarily on the q_n in what follows.

13.2.1.1 Systems Having a Few Number of Degrees of Freedom (dof)

In this section, coupled systems of small dimensions are examined, in order to better understand their physical meaning.

Single dof System

Let us suppose that, for various reasons, the beam can be reduced to a single mode. In this case (13.6) reduces to:

$$\ddot{q}_1(t) + \frac{R_a\phi_1^2(L)}{m_1}\dot{q}_1(t) + \omega_1^2 q_1(t) = 0. \tag{13.7}$$

This is simply the equation of a damped oscillator (see Chap. 2) where the dimensionless damping factor ζ_1 is

$$2\zeta_1\omega_1 = \frac{R_a\phi_1^2(L)}{m_1}. \tag{13.8}$$

Thus, for a single dof system loaded by a semi-infinite tube, the acoustic coupling adds a radiation damping to the structure.

2-dof System

Let us now truncate the continuous beam to its two lowest modes. In this case, (13.6) becomes

$$\begin{cases} \ddot{q}_1(t) + \omega_1^2 q_1(t) = -\frac{R_a\phi_1(L)}{m_1}[\phi_1(L)\dot{q}_1(t) + \phi_2(L)\dot{q}_2(t)], \\ \ddot{q}_2(t) + \omega_2^2 q_2(t) = -\frac{R_a\phi_2(L)}{m_2}[\phi_1(L)\dot{q}_1(t) + \phi_2(L)\dot{q}_2(t)]. \end{cases} \tag{13.9}$$

Equation (13.9) can be rewritten as:

$$\begin{cases} \ddot{q}_1 + 2\zeta_1\omega_1\dot{q}_1 + \omega_1^2 q_1 = -\frac{R_a\phi_1(L)\phi_2(L)}{m_1}\dot{q}_2 = C_{12}\dot{q}_2, \\ \ddot{q}_2 + 2\zeta_2\omega_2\dot{q}_2 + \omega_2^2 q_2 = -\frac{R_a\phi_2(L)\phi_1(L)}{m_2}\dot{q}_1 = C_{21}\dot{q}_1, \end{cases} \tag{13.10}$$

where $-m_1 C_{12} = -m_2 C_{21} = R_a\phi_2(L)\phi_1(L)$.

Several conclusions can be drawn from this result:

- Due to the acoustic radiation, damping terms $2\zeta_i\omega_i\dot{q}_i$ are introduced in both equations.
- The generalized displacements are coupled.
- In the absence of any other damping phenomena, the coupling coefficients C_{12} and C_{21} are linked by the property[2]:

$$C_{12}C_{21} = 4\zeta_1\zeta_2\omega_1\omega_2.$$

The eigenfrequencies of the system are the roots of the characteristic equation:

$$(s^2 + 2\zeta_1\omega_1 s + \omega_1^2)(s^2 + 2\zeta_2\omega_2 s + \omega_2^2) - 4\zeta_1\zeta_2\omega_1\omega_2 s^2 = 0, \tag{13.11}$$

This equation shows that the structural-acoustic coupling modifies the complex eigenfrequencies. In general, this equation can only be solved numerically. However, under the assumption of weak damping ($\zeta_1 \ll 1$ and $\zeta_2 \ll 1$), first-order approximations can be found [8].

13.2.1.2 Generalization

For a continuous system with a large number of dof, the differential system (13.6) is written:

$$\ddot{q}_n + 2\zeta_n\omega_n\dot{q}_n + \omega_n^2 q_n = \sum_{m\neq n} C_{nm}\dot{q}_m, \tag{13.12}$$

where

$$2\zeta_n\omega_n = \frac{R_a\phi_n^2(L)}{m_n} \quad \text{and} \quad C_{nm} = -\frac{R_a\phi_n(L)\phi_m(L)}{m_n}. \tag{13.13}$$

This expression shows the two main effects of the elasto-acoustic coupling seen in Fig. 13.2:

[2]Notice that this property is no longer valid if there is another structural damping inside the beam.

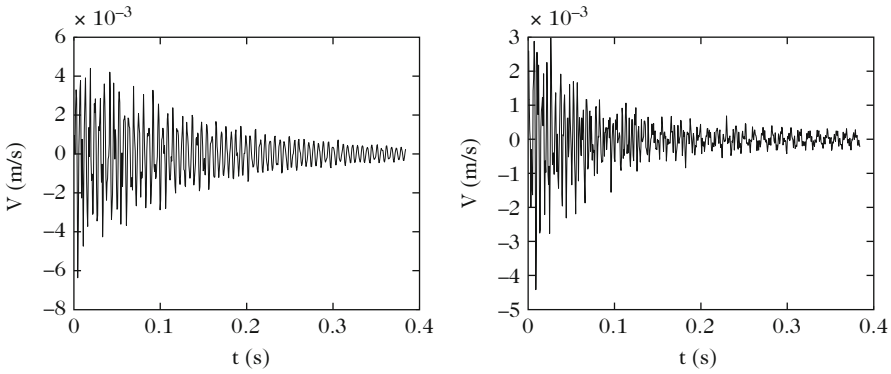

Fig. 13.3 Comparison between two velocity waveforms at a given point on a guitar soundboard (synthesis). (*Left*) Isolated mode in vacuo. (*Right*) Coupled modes due to air-soundboard coupling

1. modal damping due to radiation
2. modification of the eigenfrequencies due to intermodal coupling.

The 1-D model presented here can be further generalized to more complex systems. Figure 13.3 shows, for example, the case of a synthesized guitar tone. The picture on the left shows the time decay of an isolated mode, assuming only a modal damping in the in vacuo soundboard. The picture on the right shows the time evolution of the generalized displacement, in case of a coupling with external air and cavity. It can be seen that several other modes are excited, as a consequence of the air-structure coupling.

13.2.1.3 Reactive Effects

Imagine now that the free end of the beam subjected to longitudinal vibrations is now inserted in an infinite plane baffle, as in the case of the plane piston seen in Chap. 12. The radiation impedance now contains a real part R_a, and an imaginary part X_a.

The imaginary part corresponds to an inertial load by the fluid[3] which was not present in the case of the beam loaded by the semi-infinite tube. The main effect of X_a is to lower the eigenmodes of the structure compared to the in vacuo case.

[3]Such an effect can be taken into account as a length correction in tubes.

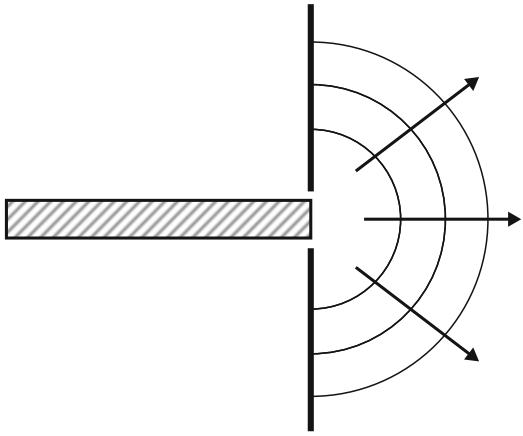

Fig. 13.4 Elastic beam vibrating longitudinally and inserted in an infinite plane baffle

13.2.2 Forced Regime

As for the harmonic oscillator in Chap. 2, the case of a forced excitation is now considered. A force $F(t)$ is applied at point $x = x_0$ with $x_0 < L$. This situation corresponds in practice to stringed instruments, where the soundboard is excited at the bridge by the vibration of a string. For a violin, the force is due to self-sustained oscillations. For a guitar or a piano, the decay times of the strings' vibrations are usually long compared to those of the soundboard, so that the excitation can be viewed as quasi-stationary. In the presence of an excitation, the energy balance (13.3) becomes

$$\int_0^L \rho_s S \left(\sum_m \phi_m(x) \ddot{q}_m(t) \right) \phi_n(x)\, dx - \int_0^L ES \left(\sum_m \phi_m''(x) q_m(t) \right) \phi_n(x)\, dx$$
$$= \int_0^L R_a \left(\sum_m \phi_m(L) \dot{q}_m(t) \right) \phi_n(x) \delta(x - L)\, dx + \int_0^L F(x_0, t) \delta(x - x_0) \phi_n(x)\, dx \tag{13.14}$$

which leads to the equations governing the generalized displacements:

$$\ddot{q}_n + 2\zeta_n \omega_n \dot{q}_n + \omega_n^2 q_n = \sum_{m \neq n} C_{nm} \dot{q}_m + F(x_0, t) \frac{\phi_n(x_0)}{m_n}, \tag{13.15}$$

or, equivalently, using the Laplace transform:

$$\tilde{q}_n(s) = H_n(s) \tilde{F}(x_0, s) + \sum_{m \neq n} K_{nm}(s) \tilde{q}_m(s), \tag{13.16}$$

with

$$H_n(s) = \frac{\phi_n(x_0)}{m_n(s^2 + 2\zeta_n\omega_n s + \omega_n^2)} \quad \text{and} \quad K_{nm}(s) = \frac{sC_{nm}}{s^2 + 2\zeta_n\omega_n s + \omega_n^2}. \tag{13.17}$$

In summary, the displacement is written:

$$\tilde{\xi}(x,s) = \sum_n \tilde{q}_n(s)\phi_n(x) = \tilde{F}(x_0,s)\sum_n \phi_n(x)H_n(s) + \sum_n \phi_n(x)\sum_{m\neq n} K_{nm}(s)\tilde{q}_m(s). \tag{13.18}$$

In matrix form, the system (13.16) is written[4]:

$$\begin{bmatrix} D_1 & -sC_{12} & \dots & -sC_{1n} \\ -sC_{21} & D_2 & \dots & -sC_{2n} \\ \dots & \dots & \dots & \dots \\ -sC_{n1} & -sC_{n2} & \dots & D_n \end{bmatrix} \begin{bmatrix} q_1 \\ q_2 \\ \dots \\ q_n \end{bmatrix} = F \begin{bmatrix} \beta_1 \\ \beta_2 \\ \dots \\ \beta_n \end{bmatrix} \tag{13.19}$$

where $\beta_n = \frac{\phi_n(x_0)}{m_n}$ and $D_n = s^2 + 2\zeta_n\omega_n s + \omega_n^2$. It is convenient to put this equation in the following form:

$$\mathbb{C}\boldsymbol{Q} = F\boldsymbol{\beta}, \tag{13.20}$$

where the displacement thus becomes

$$\xi = {}^t\boldsymbol{\phi}\boldsymbol{Q} \quad \text{where} \quad \boldsymbol{Q} = (\mathbb{C}^{-1}\boldsymbol{\beta})F. \tag{13.21}$$

Notice that, due to the sound–structure coupling, the matrix $\mathbb{C}$ is not diagonal. However, in the case of radiation in air, this coupling is generally weak and it will be justified to use approximate formulations.

13.2.2.1 Light Fluid Approximation

Several methods exist for addressing the problem of elasto-acoustic coupling in light fluid. In the method retained below, dimensionless intermodal coupling coefficients are viewed as perturbation terms, compared to the reference in vacuo case. A simple expression is then derived for the structural shapes. As previously, the presentation starts with a simple 2-dof system.

[4] In what follows, the symbols "~" will be omitted for clarity.

2-dof System

For a 2-dof system, the matrix $\mathbb{C}$ is written:

$$\mathbb{C} = \begin{bmatrix} D_1 & -sC_{12} \\ -sC_{21} & D_2 \end{bmatrix}. \tag{13.22}$$

In order to test to what extent this matrix is different from the diagonal case, we look for the diagonal matrix $\mathbb{D}$ built with the eigenvalues λ_1 and λ_2 which are solutions of the characteristic equation:

$$\begin{vmatrix} D_1 - \lambda & -sC12 \\ -sC_{21} & D_2 - \lambda \end{vmatrix} = (D_2 - \lambda)(D_1 - \lambda) - s^2 C_{12} C_{21} = 0. \tag{13.23}$$

Denoting $\mathbf{e}_i$ the corresponding eigenvectors, and $\mathbb{T} = [\mathbf{e}_1 \quad \mathbf{e}_2]$, the classical matrix relationships are obtained

$$\mathbb{T}\mathbb{D} = \mathbb{C}\mathbb{T} \quad \Leftrightarrow \quad \mathbb{D} = \mathbb{T}^{-1}\mathbb{C}\mathbb{T}, \tag{13.24}$$

where it is assumed that $\mathbb{C}$ is reversible. In the general case (without approximations), the eigenvalues of $\mathbb{C}$ are given by:

$$\lambda_{1,2} = \frac{1}{2}\left[D_1 + D_2 \pm \sqrt{(D_1 - D_2)^2 + 4s^2 C_{12} C_{21}}\right]. \tag{13.25}$$

At this stage, the following *dimensionless coupling coefficient* is defined[5]

$$\varepsilon = \frac{C_{12}C_{21}}{D_2 - D_1} = \frac{C_{12}C_{21}}{\omega_2^2 - \omega_1^2 + 2s(\zeta_2\omega_2 - \zeta_1\omega_1)}, \tag{13.26}$$

so that, for $\varepsilon \ll 1$, the eigenvalues of $\mathbb{C}$ can be written to first-order approximation:

$$\lambda_1 = D_1 - \varepsilon s^2 \quad ; \quad \lambda_2 = D_2 + \varepsilon s^2. \tag{13.27}$$

Discussion At this stage, we make the approximation of "light fluid," i.e., we assume that the coefficients C_{ij} and ζ_i are small in (13.26). As a consequence, it can be seen that the coupling parameter ε is small only under the condition that the in vacuo frequencies of the structure are sufficiently far apart from each other. If this latter condition is not fulfilled, a strong coupling can be observed, even for a light fluid. Such a situation occurs, for example, in the coupling between the fundamental mode of a head, and the lowest mode of the cavity in timpani (see Chap. 14).

[5] See also the definition of a coupling coefficient in Sect. 6.4 of Chap. 6.

Generalization

For a system with n dof, it can be shown that the first-order approximations of the eigenvalues λ_i can be written as:

$$\lambda_i = D_i + \varepsilon_i s^2 \quad \text{with} \quad \varepsilon_i = \sum_j \frac{C_{ij}C_{ji}}{D_i - D_j} \quad \text{and} \quad 1 \leq j \leq n \quad \text{and} \quad j \neq i. \tag{13.28}$$

In summary, n intermodal coupling coefficients are defined, one for each pair of modes. The conditions of weak coupling are generalized: light fluid and sufficient distance between the values of the eigenfrequencies.

13.2.2.2 Operating Deflexion Shapes

Forced excitation is often used for measurements purpose on musical instruments. In case of uncoupled modes, a forced excitation close to one particular eigenfrequency of the structure yields the corresponding modal shape. However for coupled modes, as in the case examined in this section, the observed deflexion cannot be reduced to a single modal shape. They are usually referred to as ODS.

In what follows, we content ourselves with a simplified presentation with two dof. The results can be generalized to any number n of dof. We start by writing the displacement field of the structure in vacuo:

$$\xi_0 = \phi_{10} q_{10} + \phi_{20} q_{20}. \tag{13.29}$$

For the same structure vibrating in air, and using an expansion of the displacement on the *in vacuo modes*, we get

$$\xi = \phi_{10} q_1 + \phi_{20} q_2. \tag{13.30}$$

Based on the results obtained in the previous section, we can write to the first-order:

$$\xi = \phi_{10}\left(q_{10} + \frac{sC_{12}}{D_1} q_{20}\right) + \phi_{20}\left(q_{20} + q_{10}\frac{sC_{21}}{D_2}\right), \tag{13.31}$$

or, equivalently, by grouping the terms corresponding to each generalized displacement:

$$\xi = q_{10}\left(\phi_{10} + \frac{sC_{21}}{D_2}\phi_{20}\right) + q_{20}\left(\phi_{20} + \phi_{10}\frac{sC_{12}}{D_1}\right) \quad \text{with} \quad q_{i0} = \frac{\phi_{i0}}{m_i D_i} F. \tag{13.32}$$

Let us now examine typical experimental situations where a sinusoidal force $F(t) = F_0 H(t) \sin \omega t$[6] is applied suddenly at time $t = 0$ and at point x_0.

(1) In the particular case where both the frequency and excitation point are selected so that q_{20} is negligible compared to q_{10}, the displacement becomes

$$\phi_1 = \phi_{10} + \phi_{20} \frac{sC_{21}}{D_2}. \tag{13.33}$$

After a certain amount of time, the second term in (13.33) tends to zero, and the observed deflexion corresponds to the first mode.

(2) However, in the general case, Eq. (13.32) shows that both modes are simultaneously excited. After the transient regime, the stationary solution for the displacement is given by:

$$\xi(\omega, x) = \left[\frac{\phi_{10}\beta_1}{D_1(j\omega)} + \frac{\phi_{20}\beta_2}{D_2(j\omega)} \right]. \tag{13.34}$$

The quantity enclosed in square brackets is the ODS of the structure at frequency ω.

13.2.3 Energy Approach

In the previous sections, the internal losses inside the material of the structure were not considered. However, if we take the example of a stringed instrument, only a part of the mechanical power transmitted by the string to the body is transformed into acoustic power. The difference is essentially due to dissipation in the material.

The energy balance and the acoustical efficiency of a single dof oscillator loaded by a tube filled with air were determined in Chap. 2. This example is generalized here to a structural system with multiple dof coupled to a fluid. For a better comprehension, we start with a 2-dof system. The losses in the structure itself are represented by two mechanical resistances r_1 and r_2. The resistances r_{a1} and r_{a2} account for the radiation losses. One goal is to compare the dissipated power in the structure and in air, respectively.

13.2.3.1 Structural and Acoustic Resistance Matrix

The illustrating example is still the case of a longitudinally vibrating beam radiating at one end ($x = L$) in a semi-infinite tube (see Fig. 13.2). The excitation force F is applied at point $x = x_0$. The radiation coupling coefficients are defined in (13.13).

[6] Recall that $H(t)$ is the Heaviside function.

The system is truncated to the first two modes of the beam, for simplicity. The system of equations governing the system is

$$\begin{cases} m_1\ddot{q}_1 + (r_1 + r_{a1})\dot{q}_1 + k_1 q_1 + \gamma\dot{q}_2 = \phi_1(x_0)F, \\ m_2\ddot{q}_2 + (r_2 + r_{a2})\dot{q}_2 + k_1 q_2 + \gamma\dot{q}_1 = \phi_2(x_0)F, \end{cases} \tag{13.35}$$

where $\gamma = -C_{12}m_1 = -C_{21}m_2$. The following notations are used

$$\begin{cases} 2\zeta_1\omega_1 = \frac{r_1+r_{a1}}{m_1} \quad ; \quad 2\zeta_{10}\omega_1 = \frac{r_1}{m_1} \quad ; \quad \omega_1^2 = \frac{k_1}{m_1}, \\ 2\zeta_2\omega_2 = \frac{r_2+r_{a2}}{m_1} \quad ; \quad 2\zeta_{20}\omega_2 = \frac{r_2}{m_2} \quad ; \quad \omega_2^2 = \frac{k_2}{m_2}. \end{cases} \tag{13.36}$$

The instantaneous mechanical power imparted to the beam is

$$\begin{aligned} p_m(t) &= F\frac{d\xi}{dt}(x_0, t) = F\left[\phi_1(x_0)\dot{q}_1 + \phi_2(x_0)\dot{q}_2\right] \\ &= m_1\ddot{q}_1\dot{q}_1 + (r_1 + r_{a1})\dot{q}_1^2 + k_1 q_1\dot{q}_1 + 2\gamma\dot{q}_1\dot{q}_2 \\ &\quad + m_2\ddot{q}_2\dot{q}_2 + (r_2 + r_{a2})\dot{q}_2^2 + k_2 q_2\dot{q}_2. \end{aligned} \tag{13.37}$$

In case of a periodic motion with period T, the mean value of this power is:

$$\mathscr{P}_m(T) = \frac{1}{T}\int_0^T (r_1 + r_{a1})\dot{q}_1^2 + (r_2 + r_{a2})\dot{q}_2^2 + 2\gamma\dot{q}_2\dot{q}_1\, dt, \tag{13.38}$$

It is composed of three terms:

- The mean power dissipate in the structure (material) $\mathscr{P}_s(T) = \frac{1}{T}\int_0^T r_1\dot{q}_1^2 + r_2\dot{q}_2^2\, dt$,
- The mean radiated acoustic power $\mathscr{P}_a(T) = \frac{1}{T}\int_0^T r_{a1}\dot{q}_1^2 + r_{a2}\dot{q}_2^2\, dt$,
- The mean coupling power $\mathscr{P}_c(T) = \frac{2}{T}\int_0^T \gamma\dot{q}_2\dot{q}_1\, dt$ reflecting the energy exchange between the modes.

In the particular case of sinusoidal excitation, we get

$$\mathscr{P}_m = \frac{1}{2}\left[(r_1 + r_{a1})|\dot{q}_1|^2 + (r_2 + r_{a2})|\dot{q}_2|^2 + 2\gamma|\dot{q}_2||\dot{q}_1|\right]. \tag{13.39}$$

In vacuo, this expression reduces to:

$$\mathscr{P}_{mo} = \frac{1}{2}\left[r_1|\dot{q}_{10}|^2 + r_2|\dot{q}_{20}|^2\right]. \tag{13.40}$$

In what follows, it is convenient to write these results in matrix form. Introducing the notations: $\dot{\mathbf{Q}} = \begin{bmatrix} \dot{q}_1 \\ \dot{q}_2 \end{bmatrix}$, $\mathbb{R}_s = \begin{bmatrix} r_1 & 0 \\ 0 & r_2 \end{bmatrix}$ and $\mathbb{R}_a = \begin{bmatrix} r_{a1} & \gamma \\ \gamma & r_{a2} \end{bmatrix}$, we get

$$\mathscr{P}_m = \dot{\mathbf{Q}}^H \left[\mathbb{R}_s + \mathbb{R}_a\right] \dot{\mathbf{Q}}, \tag{13.41}$$

where $\dot{\mathbf{Q}}^H$ is the Hermitian conjugate (conjugate transpose) of $\dot{\mathbf{Q}}$. $\mathbb{R}_s$ is the matrix of the structural resistances. For the sake of simplicity, it is written here in diagonal form. However, it is not the case for all causes of damping (see Chap. 5). Finally, $\mathbb{R}_a$ is the radiation resistance matrix of the beam coupled to the fluid.

13.2.3.2 Generalization and Acoustical Efficiency

Generalizing the previous results to the n dof of the beam, we find

$$\mathscr{P}_m(T) = \frac{1}{T}\int_0^T \left[\sum_{i=1}^{n}(r_i + r_{ai})\dot{q}_i^2 + \sum_{i=1}^{n}\sum_{j\neq i=1}^{n} \gamma_{ij}\dot{q}_i\dot{q}_j\right] dt \quad \text{où} \quad \gamma_{ij} = -m_i C_{ij}. \tag{13.42}$$

The resistance matrix becomes

$$\mathbb{R}_s + \mathbb{R}_a = \begin{bmatrix} r_1 + r_{a1} & \dots & \gamma_{1i} & \dots & \gamma_{1j} & \dots & \gamma_{1n} \\ \dots & \dots & \dots & \dots & \dots & \dots & \dots \\ \gamma_{i1} & \dots & r_i + r_{ai} & \dots & \gamma_{ij} & \dots & \gamma_{in} \\ \dots & \dots & \dots & \dots & \dots & \dots & \dots \\ \gamma_{j1} & \dots & \gamma_{ji} & \dots & r_j + r_{aj} & \dots & \gamma_{jn} \\ \dots & \dots & \dots & \dots & \dots & \dots & \dots \\ \gamma_{n1} & \dots & \gamma_{ni} & \dots & \gamma_{nj} & \dots & r_n + r_{an}. \end{bmatrix} \tag{13.43}$$

The radiated acoustic power is given by:

$$\mathscr{P}_a = \dot{\mathbf{Q}}^H \mathbb{R}_a \dot{\mathbf{Q}}. \tag{13.44}$$

In conclusion, for an elastic-acoustic system where the modes are coupled by the radiation, the acoustical efficiency is written:

$$\eta_m = \frac{\dot{\mathbf{Q}}^H \left[\mathbb{R}_a\right] \dot{\mathbf{Q}}}{\dot{\mathbf{Q}}^H \left[\mathbb{R}_s + \mathbb{R}_a\right] \dot{\mathbf{Q}}}. \tag{13.45}$$

Equation (13.45) is thus the generalization of the result obtained in Chap. 2 for a single oscillator coupled to the air.

Measurements conducted on a number of classical guitars have shown that the order of magnitude of the acoustical efficiency is nearly 10 % between 100 and 1000 Hz, and 5 % between 1 and 8 kHz. However, for some particular frequencies, the efficiency can reach 20 % [5].

13.3 Radiation of an Infinite Thin Plate

13.3.1 Elastic Equation

The radiation properties of a plane surface with uniform velocity profile were studied in Chap. 12. This theory is valid for the structures subjected to rigid body motion. It can also be applied to the radiation of a hole (as the soundhole of a guitar, for example), as long as the normal acoustic velocity remains constant over the cross-section.

As soon as the frequency increases, which causes in turn that the vibratory wavelength becomes comparable to (or smaller than) the dimensions of the structure, then one has to consider the propagation phenomena inside the structure. To illustrate this point, the case of flexural motion of thin plates is treated below.

The presentation starts with the case of an "infinite" plate, which amounts to neglecting the reflection of waves at the edges. The particular case of an isotropic plate subjected to a transverse velocity $V(x,\omega) = V_0(\omega)e^{-jk_B x}$ along the x-axis is studied in the frequency domain. $k_B = 2\pi/\lambda_B$ is the flexural wavenumber (see Fig. 13.5). For a given frequency ω, the phase velocity of the elastic wave in the plate is given by $c_B = \omega/k_B$.

At this stage, the internal losses in the plate, and the reaction of the acoustic pressure on it, are left temporarily aside. These features will be progressively introduced later. ρ_p is the density of the plate, E its Young's modulus, ν its Poisson's coefficient, and h its thickness. In the context of the Kirchhoff–Love assumptions, it has been shown in Chap. 1 that the governing equation of motion for the plate is given by:

$$-\omega^2\rho_p hW + D\frac{d^4W}{dx^4} = 0 \quad \text{with} \quad D = \frac{Eh^3}{12(1-\nu^2)}, \tag{13.46}$$

where $W(x,\omega)$ is the transverse displacement.

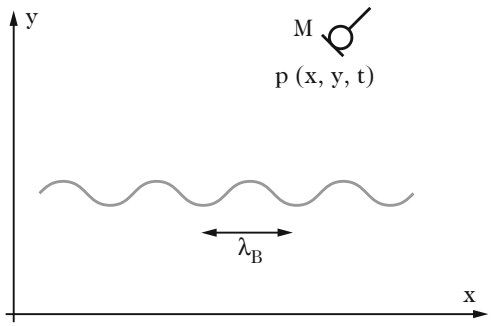

Fig. 13.5 Radiation of an infinite plate subjected to transverse flexural vibrations. The elastic flexural wavelength is λ_B. The objective is to determine the pressure p radiated by this plate in free space. For simplicity, the case of a "1D" plate (equivalent to a beam) is considered. As a consequence, the pressure only depends on two spatial coordinates: x and y

13.3.2 Acoustic Equations

The Helmholtz equation governing the sound pressure $P(x, y, \omega)$ is written:

$$\frac{\partial^2 P}{\partial x^2} + \frac{\partial^2 P}{\partial y^2} + k^2 P = 0. \tag{13.47}$$

The elasto-acoustic interaction between the plate and the air (with density ρ) is ensured by the continuity equation for the normal velocities:

$$\left.\frac{\partial P}{\partial y}\right|_{y=0} = -j\omega\rho V_0 e^{-jk_B x}. \tag{13.48}$$

13.3.3 Dispersion Equations and Critical Frequency

For any progressive flexural wave of the form $e^{j(\omega t - k_B x)}$ injected in Eq. (13.46), we get the dispersion relationship between frequency and wavenumber in the plate:

$$\omega = \sqrt{\frac{D}{\rho_p h}} k_B^2. \tag{13.49}$$

Due to the linearity of the problem, the same frequency is found in the acoustic field, which yields the acoustic dispersion relation:

$$\omega = kc. \tag{13.50}$$

where c is the speed of sound in air. Plotting both dispersion relationships (13.49) and (13.50) on the same figure (see Fig. 13.6) shows that a particular frequency exists for which the wavenumber in the plate is equal to the wavenumber in air. This so-called *critical (or coincidence) frequency* is given by:

$$f_c = \frac{\omega_c}{2\pi} = \frac{c^2}{2\pi}\sqrt{\frac{\rho_p h}{D}} = \frac{c^2}{\pi h}\sqrt{\frac{3\rho_p(1-\nu^2)}{E}}. \tag{13.51}$$

The critical frequency f_c plays a major role in elasto-acoustic coupling. In Sect. 13.3.4, it will be shown that this two distinct frequency domains are defined by this frequency: below f_c, the radiation efficiency is weak, whereas it becomes significant for frequencies higher than f_c. A maximum is obtained for the particular case $f = f_c$. This result is due to the particular shape (parabolic, here) of the plate dispersion. By contrast, for ideal membranes, the dispersion relationship is linear, and no critical frequency can be exhibited. There is only one particular case where both wave speed in air and in the membrane are equal (see the next paragraph).

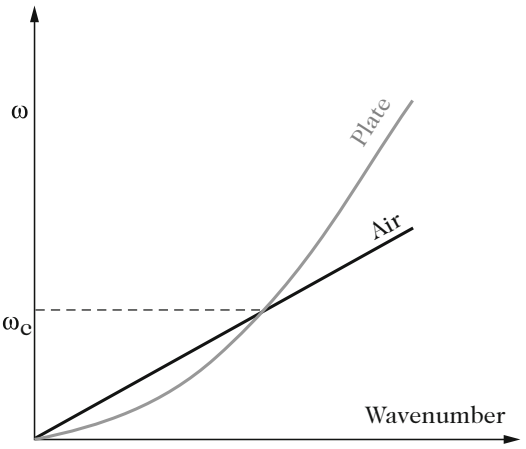

Fig. 13.6 Equations of dispersion in plate and air. The critical (or coincidence) frequency is given by the intersection of both curves

For other structures (for some shells, for example) some situations can also be observed where there are no intersections between the air and structures dispersion relationships. These features will be studied in more details in Sect. 13.5.

In Eq. (13.51), it can be seen that the critical frequency depends on the thickness of the plate and on the material properties. In summary, the critical frequency decreases as the plate becomes thicker, more dense, and more rigid.

Transposing these results to stringed instruments, one can derive that, for similar thickness and density, replacing a given material by a more rigid one contributes to lower the critical frequency which, in turn, should enhance the radiation efficiency of the lowest notes. In this context, gluing some ribs on the soundboard contributes to increase its stiffness and its mean thickness, which is coherent with a decrease of the critical frequency. However, one must be careful before concluding that these modifications will, in fact, lead to an increase in sound power. One has first to consider (and estimate) the change of velocity profile of the soundboard due to the attachment of ribs.

Critical Domain for Orthotropic Materials

For orthotropic materials (such as the wood species used for stringed instruments), the calculation (13.51) can be conducted again in the two limiting cases corresponding to the stiffer and to the more flexible directions, respectively. Two dispersion curves are then obtained from which the critical domain $[\omega_{c1}, \omega_{c2}]$ is derived (see Fig. 13.7). It has been shown in Chap. 3 that, for a finite orthotropic plate, all eigenfrequencies are situated between the two dispersion curves. Among these eigenfrequencies, those situated in the critical interval will have a particularly high radiation efficiency.

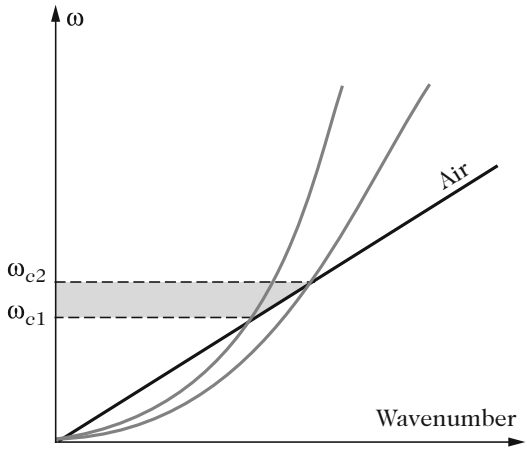

Fig. 13.7 Critical domain for the orthotropic materials. The *straight line* accounts for the air dispersion. The direction of maximal rigidity determines the frequency ω_{c1}, whereas the less stiff direction determines ω_{c2}. The "critical domain" is given by the interval $[\omega_{c1}, \omega_{c2}]$

Critical Frequency for Stiff Membranes and Prestressed Plates

The flexural motion of ideal membranes (with no damping and stiffness terms) is governed by a wave equation. As a consequence, their dispersion equation is of the form $\omega = kc_m$, where $c_m = \sqrt{\tau/\rho_m h}$ is the transverse wave speed (see Chap. 1). In timpani membranes, the tension and density are such that usually we have $c_m < c$. In practice, the wave speed is of the order of $100\,\mathrm{m\,s^{-1}}$ for timpani.

As a consequence, the dispersion curve of the membrane is a straight line with a lower slope than for the air, and there is no intersection between both curves (see Fig. 13.8). In practice, however, timpani heads (like nylon guitar strings) have a nonzero elasticity modulus. Therefore, the dispersion equation is written:

$$\omega = \sqrt{\frac{Dk^4 + \tau k^2}{\rho_m h}}, \tag{13.52}$$

and it becomes possible to define a critical frequency. The dispersion equation for a prestressed plate is written in the form similar to (13.52). If the plate is subjected to a compression ($\tau < 0$), then its critical frequency increases. Conversely, if the plate is subjected to a tension ($\tau > 0$), its critical frequency decreases. In conclusion, it is checked on this example that introducing any kind of stiffening effect in the plate globally contributes to yield favorable conditions for the radiation.

13.3.4 Pressure, Velocity, and Acoustic Power

In order to show the relevance of the critical frequency on the radiation efficiency, for the infinite plane plate in air, both the pressure and acoustic velocity in the fluid

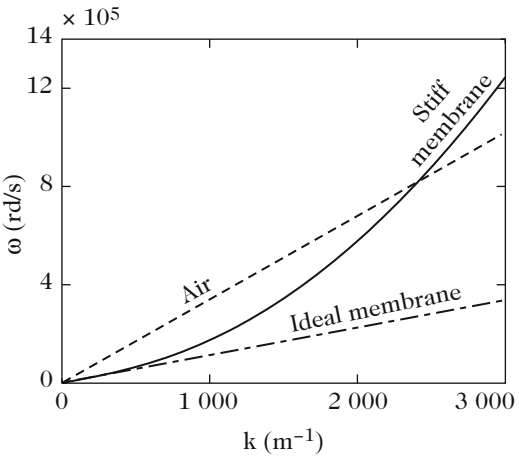

Fig. 13.8 Dispersion curves for stiff membranes and prestressed plates. *Dashed line*: air dispersion. *Dash-dotted line*: dispersion curve of an ideal membrane with density $\rho_m = 1.05 \times 10^3$ kg m^{-3}, thickness $h = 0.25$ mm, and tension $\tau = 3325$ N m^{-1}. *Solid line*: dispersion of the same membrane taking the Young's modulus $E = 3 \times 10^9$ N m^{-2} and the Poisson's coefficient $\nu = 0.4$ into account. Notice that, in this latter case, a critical frequency exists though it has a rather high frequency (127 kHz)

need to be calculated explicitly. This, in turn, will allow the calculation of sound intensity and acoustic power.

We look for a pressure field of the form $P(x, y) = P_0 e^{-j(k_x x + k_y y)}$. The Helmholtz equation (13.47) then yields $k^2 = k_x^2 + k_y^2$. In addition, the condition of continuity on the plate (13.48) imposes $k_x = k_B$, so that:

$$k_y^2 = k^2 - k_B^2 \quad \text{and} \quad P_0 = \rho c V_0 \frac{k}{k_y}. \tag{13.53}$$

As a consequence, the pressure and velocity fields are written:

$$\begin{cases} P(x, y, \omega) = \rho c V_0 \dfrac{k}{k_y} e^{-j(k_x x + k_y y)}, \\ V_x(x, y, \omega) = -\dfrac{1}{j\omega\rho} \dfrac{\partial P}{\partial x} = V_0 \dfrac{k_B}{k_y} e^{-j(k_x x + k_y y)}, \\ V_y(x, y, \omega) = -\dfrac{1}{j\omega\rho} \dfrac{\partial P}{\partial y} = V_0 e^{-j(k_x x + k_y y)}. \end{cases} \tag{13.54}$$

The first equation in (13.53) shows that the k_y component of the wavenumber is real if $k > k_B$, and purely imaginary otherwise.

For a given frequency, the first so-called *supersonic* case is obtained when the acoustic wavelength $\lambda = 2\pi/k$ is less than the elastic wavelength $\lambda_B = 2\pi/k_B$.

Figure 13.6 shows that this situation is obtained when the frequency of vibration of the plate is higher than its critical frequency. In terms of wave speed, this amounts to saying that $c_B = \omega/k_B > c = \omega/k$, which justifies the designation of *supersonic*. Conversely, when the acoustic wavelength $\lambda = 2\pi/k$ is higher than the elastic wavelength in the plate $\lambda_B = 2\pi/k_B$ or, equivalently, when the driving frequency is less than the critical frequency, the elastic wave speed is lower than the speed of sound, and this corresponds to the so-called *subsonic* case. These two situations are now examined with more details.

13.3.4.1 Supersonic Case

The supersonic case is illustrated in Fig. 13.9. With $k_y = \sqrt{k^2 - k_B^2}$, the pressure is written:

$$P(x, y) = \rho c V_0 \frac{k}{\sqrt{k^2 - k_B^2}} e^{-j(k_B x + \sqrt{k^2 - k_B^2} y)}. \tag{13.55}$$

The wave vector (indication the direction of propagation) is given by the angle θ defined by:

$$\sin\theta = \frac{k_B}{k} = \sqrt{\frac{\omega_c}{\omega}}. \tag{13.56}$$

As the frequency increases, the angle θ between the direction of propagation and the vector normal to the plate decreases. The direction of propagation then tends

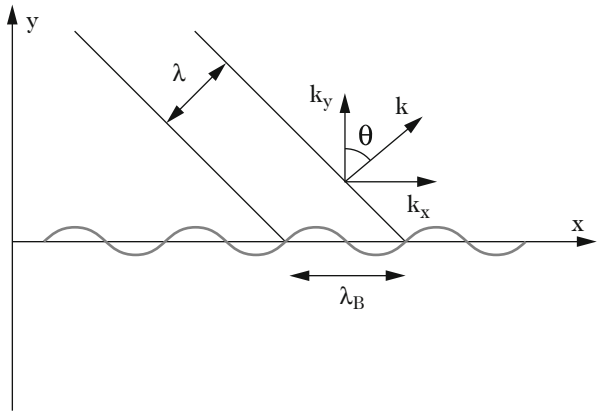

Fig. 13.9 Supersonic case. When the acoustic wavelength λ is less than the elastic wavelength λ_B in the plate, the acoustic wave radiated by the plate propagates in the direction θ. As the frequency increases, the angle θ decreases, and thus the propagation tends to be more and more perpendicular to the plate

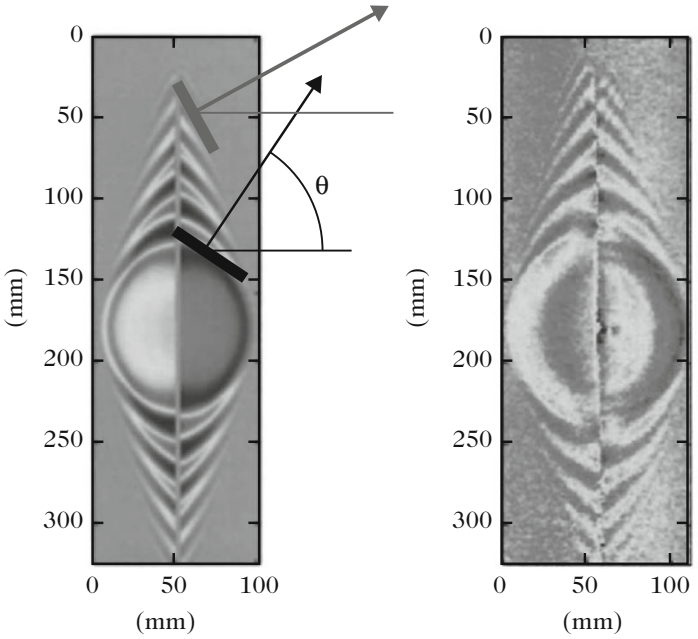

Fig. 13.10 Radiation of a plate excited by an impact in its center. (*Left*) simulation. (*Right*) measurements. The plate is perpendicular to the plane of the figure. The angle θ between the direction of propagation and the vector normal to the plate decreases from the center to the edges, consecutive to the increase of propagation speed with frequency. See also the insert on the "optical measurements of sound fields" in the next section. After [32]

to become progressively perpendicular to the plate. In contrast, as the vibration frequency decreases and tends to the critical frequency of the plate (with $f \geq f_c$), then the acoustic wave progressively tends to be confined to the plate plane.[7]

This property is clearly visible in Fig. 13.10 which shows a comparison between measurements and simulation for a plate excited by an impact in its center. As a

[7]Here, an interesting link can be made with the linear array of monopoles shown in Fig. 12.7. It was shown in the previous chapter that, as the number N of monopoles tend to infinity, then the direction of radiation tends to $\Theta = 0$, which is equivalent to $kd\cos\theta = \varphi$. This can only occur under the condition $|\varphi| < kd$. In the present example of the plate, the definition of the angle θ is modified, so that we must here convert the $\cos\theta$ of the monopole array in $\sin\theta$, which yields

$$\sin\theta = \frac{\varphi}{kd}.$$

For the plate, the phase shift φ between two consecutive "monopoles" is given here by $k_B d = \varphi$. As d tends to zero, we find Eq. (13.56) again. This shows that the linear array of monopoles is of the *supersonic* type. We can further add that if a condition such as $|\varphi| > kd$ would have been obtained as N tends to infinity, then no radiation would have exist in the far field, because Θ could not be zero. This remark will be useful in Chap. 14 to understand why there is no critical frequency in wind instruments.

result of the impact force, flexural waves propagate from the center to the edges. According to the elastic dispersion relationship, the high frequencies propagate faster than the low frequencies. For this reason, the angle θ between the vector normal to the plate and the direction of propagation decreases from the impact point to the edge.

The mean value of the acoustic power radiated per unit area is obtained by a classical method:

$$\langle \mathscr{P}_a \rangle = \frac{1}{2}\mathscr{R}e\{PV_y^\star\} = \frac{1}{2}\rho c V_0^2 \frac{k}{\sqrt{k^2 - k_B^2}} = \frac{1}{2}\rho c V_0^2 \frac{1}{\sqrt{1 - \frac{\omega_c}{\omega}}}. \tag{13.57}$$

The *radiation efficiency* $\sigma(\omega)$ is defined as the ratio between the mean value of the power radiated by the plate and the power obtained for an identical plate with the same area vibrating with a uniform velocity V_0. Here, we have (see Fig. 13.11):

$$\sigma = \frac{\langle \mathscr{P}_a \rangle}{\frac{1}{2}\rho c V_0^2} = \frac{k}{\sqrt{k^2 - k_B^2}} = \frac{1}{\sqrt{1 - \frac{\omega_c}{\omega}}}. \tag{13.58}$$

In summary, it has been shown that the infinite plate can radiate acoustic energy for the frequencies above the critical frequency. As the frequency $f > f_c$ becomes closer to the critical frequency, then the radiation efficiency increases and the direction of propagation tends to the plate plane. Notice that the simple theory presented here predicts that $\langle \mathscr{P}_a \rangle$ can tend to infinity. In the reality, the acoustic power is bounded both by the internal losses and by the finite size of the plate, as shown in the next sections.

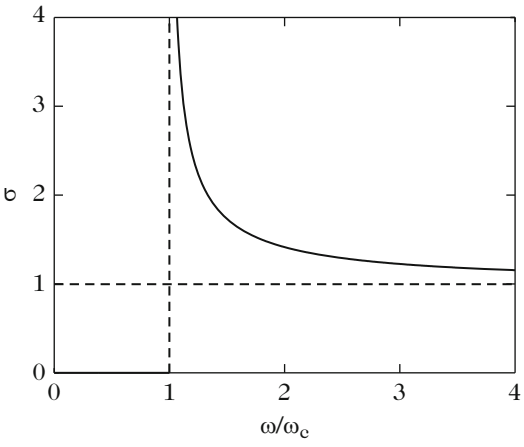

Fig. 13.11 Radiation efficiency of the infinite plate as a function of frequency

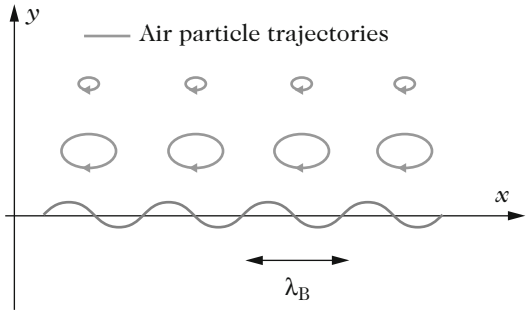

Fig. 13.12 Subsonic case. The trajectories of the air particles are elliptic, with axes decreasing exponentially with the distance from the plate plane

13.3.4.2 Subsonic Case

The subsonic case corresponds to the situation shown in Fig. 13.12. In this case, we have $k_y = -j\sqrt{k_B^2 - k^2}$, and the acoustic variables are written:

$$\begin{cases} P(x,y) = j\rho c V_0 \dfrac{k}{\sqrt{k_B^2 - k^2}} e^{-jk_B x} e^{-\sqrt{k_B^2 - k^2}\,y}, \\ V_x(x,y) = jV_0 \dfrac{k_B}{\sqrt{k_B^2 - k^2}} e^{-jk_B x} e^{-\sqrt{k_B^2 - k^2}\,y}, \\ V_y(x,y) = V_0 e^{-jk_B x} e^{-\sqrt{k_B^2 - k^2}\,y}. \end{cases} \tag{13.59}$$

The pressure modulus decreases exponentially with the distance y. The exponent increases with the ratio between the acoustic wavelength and the elastic wavelength. From a physical point of view, this means that there is destructive interferences between the neighboring "dipoles" of the plate over one given acoustic wavelength λ.

Examining now the acoustic velocity sheds useful light on the underlying physics of the subsonic case. It is seen in Eq. (13.59) that both components of the velocity vector are in quadrature and, in general, with different amplitudes. As a consequence the trajectories of the particles are elliptic. The motion is then confined locally and there is no transmission of energy from plane to plane as in the propagative case. In addition, the area of the ellipses decrease exponentially with the distance to the plate. The quantity $1/\sqrt{k_B^2 - k^2}$ gives a measure of the "thickness" of this evanescent field. It can be seen that this thickness decreases as the two wavelengths (elastic and acoustic) are more and more apart from each other. Finally, one can easily check that the mean value of the acoustic power $\langle \mathscr{P}_a \rangle$ is zero in the subsonic case, since the product $PV_y^\star$ is purely imaginary.

Let us now conclude this paragraph with the description of an experiment. It can be observed that if a second plate made of porous (absorbing) material is

placed close to the first vibrating plate, then the radiation losses increase, which induces an increase of damping for the elastic vibrations in the first plate. In order to demonstrate this phenomenon in a rigorous manner, the reader is invited to reconsider the previous mathematical derivations with a complex structural wavenumber k_B [10]. In short, this additional damping is due to the fact that, close to the plate, the energy contained in the elliptic motion of the particles is transformed into heat in the porous material. Benefit of this well-known phenomenon was taken, for example, in the plate reverberators used in the past in the recording studio for adding artificial reverberation effects [2].

Optical Measurements of Sound Fields

The figure shown in Fig. 13.10-(right) was obtained by means of optical measurements of the acoustic pressure [32]. A first instantaneous image of the sound field is made with a laser, for the air at rest. In this case, the optical index is n_0. A rubber bullet then hits the plate: as a result a transient sound pressure p is generated in the vicinity of the plate. A second image is recorded with the same laser, at a very short time t after the impact. In accordance with the Gladstone–Dale law, the optical index field is then governed by the equation:

$$n - 1 = K\rho, \tag{13.60}$$

where K is the Gladstone constant, and ρ the density of the fluid. The density is linked to the sound pressure by the adiabatic equation of state (see Chap. 1). Due to the index variation consecutive to the propagation of the sound wave, the optical path in the z-direction (the plane of Fig. 13.10) is modified by the quantity:

$$\Delta L = \int [n(x, y, z) - n_0]\ dz. \tag{13.61}$$

As a consequence, the phase shift undergone by the laser beam with wavenumber k_l is $\Delta\Phi = k_l \Delta L$. The superposition of both images generates the fringes of interference shown in Fig. 13.10.

13.3.5 Acoustic Loading of the Plate

As for the pulsating sphere in the previous chapter, the radiation impedance (or acoustic loading impedance) per unit area of the plate is defined by the ratio of the pressure divided by the normal acoustic velocity in the plate plane (in $y = 0$). For the supersonic case, Eq. (13.55) yields

$$Z(x,0) = \rho c \frac{k}{\sqrt{k^2 - k_B^2}} = \rho c \frac{1}{\sqrt{1 - \frac{\omega_c}{\omega}}}, \tag{13.62}$$

Since k is larger than k_B, the radiation impedance is purely resistive and equal to $R_a = \rho c \sigma(\omega)$. This radiation resistance is thus proportional to the radiation efficiency. Conversely, in the subsonic case, a purely imaginary radiation impedance is obtained

$$Z(x,0) = \rho c \frac{jk}{\sqrt{k_B^2 - k^2}} = j\rho\omega \frac{1}{\sqrt{k_B^2 - k^2}}. \tag{13.63}$$

which corresponds to an acoustic mass of the form:

$$M_a = \rho \frac{1}{\sqrt{k_B^2 - k^2}}, \tag{13.64}$$

This result quantifies the inertial loading of the fluid on the plate.

Remark. In this paragraph, only the radiation on one side of the plate was considered, in the positive half-space. In reality, notice that the infinite plate also radiates another sound field, in opposite phase, in the negative half-space.

13.3.6 Dispersion Equation for the Acoustically Loaded Plate

In order to evaluate and quantify the influence of the acoustic field on the plate, its flexural equation of motion needs to be modified through introduction of the pressure forces on each side of the plate, as follows:

$$-\omega^2 \rho_p h W + D \frac{d^4 W}{dx^4} = -P(x,0^+,\omega) + P(x,0^-,\omega). \tag{13.65}$$

As previously, the pressure terms are governed by the Helmholtz equation, and the continuity of the normal velocity is expressed by means of the Euler equation. These classical derivations are not detailed here. It is assumed that the plate radiates in the air on both sides.

The demonstration is conducted in the case of a forcing frequency ω. The unknown is the flexural wave number, denoted γ_B in order to make a distinction with the case presented in Sect. 13.3.4 where the acoustic loading was ignored. According to the results obtained in Eq. (13.54), the equation of dispersion becomes

$$D(\gamma_B,\omega) = -\frac{2j\rho}{\sqrt{k^2 - \gamma_B^2}} + \rho_p h \left(1 - \frac{D\gamma_B^4}{\rho_p h \omega^2}\right) = 0. \tag{13.66}$$

The first term in Eq. (13.66) accounts for the acoustic loading of the fluid. If the plate radiates in a light fluid (which is usually the case for a fluid with a "small" density ρ compared to the density of the plate), then we have $\gamma_B \simeq k_B$ (see Sect. 13.3.3).

It is often of interest to write the equation of dispersion (13.66) in a dimensionless form, using the following reduced variables:

$$\Omega = \frac{\omega}{\omega_c} \quad ; \quad \tau = \sqrt{\frac{c^2}{c_b^2} - 1} \quad ; \quad \varepsilon = \frac{2\rho c}{\omega_c \rho_p h}, \tag{13.67}$$

where $c_b = \omega/\gamma_B$ is the speed of the flexural waves for the acoustically loaded plated. After some derivations, the following equation is obtained [21]:

$$\tau^5 + 2\tau^3 + \left(1 - \Omega^{-2}\right)\tau - \varepsilon\Omega^{-3} = 0. \tag{13.68}$$

It can be shown that Eq. (13.68) has five roots. Only two of them are physically relevant for the radiation of the loaded plate. Compared to the supersonic case presented in Sect. 13.3.4, these roots are complex, with a positive imaginary part. This means that the elastic wave is damped in the plate, due to the radiation losses.

For stringed instruments, the order of magnitude for the physical parameters are the following: $f_c = 1\,\text{kHz}$, $\rho_p = 10^3\,\text{kg/m}^3$, $h = 1\,\text{mm}$, $\rho = 1.2\,\text{kg/m}^3$, and $c = 340\,\text{m/s}$. As a consequence, the parameter ε which quantifies the acoustic loading is equal to 0.15.

13.3.7 Radiation of a Point-Excited Plate

13.3.7.1 One Step Backwards: Back to the Plate Vibrations, Ignoring the Acoustic Loading

The particular case of an infinite point-excited plate is examined below. This is a very pertinent example in musical acoustics, since it accounts well for the practical situation of a soundboard excited by a string, at least during the time interval before the first reflections at the boundaries.

The geometry of the problem is shown in Fig. 13.13. For convenience, the problem is solved in polar coordinates, taking advantage of the axial symmetry. In the Fourier domain, the flexural equation of motion is written:

$$D\left(\frac{d^2}{dr^2} + \frac{1}{r}\frac{d}{dr}\right)^2 W - \rho_p h\omega^2 W = Q(r), \tag{13.69}$$

where the source term $Q(r)$ has the dimension of a surface density of force and is defined by:

$$\int_0^{2\pi} \int_0^{\infty} Q(r) r dr d\theta = F_0, \tag{13.70}$$

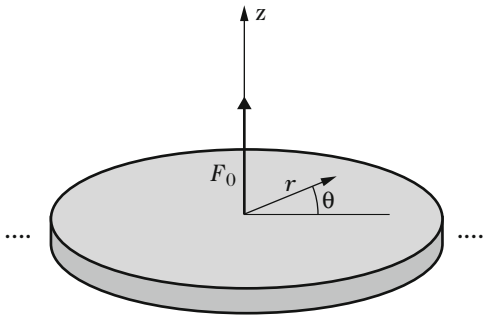

Fig. 13.13 Point-excited vibrating plate

which yields

$$Q(r) = \frac{F_0 \delta(r)}{2\pi r}. \tag{13.71}$$

This class of axisymmetrical problem can be solved with the Hankel transform of zero-order, defined as:

$$\hat{f}(\gamma) = \int_0^\infty f(r) r J_0(\gamma r) dr, \tag{13.72}$$

where J_0 is the zero-order Bessel function of the first kind [1]. Applying this transform to the equation of motion of the plate (13.69) yields the Hankel function of the displacement:

$$\hat{W}(\gamma) = \frac{F_0}{2\pi} \frac{1}{D\left(\gamma^4 - k_B^4\right)} \quad \text{with} \quad k_B^4 = \frac{\rho_p h \omega^2}{D}. \tag{13.73}$$

The plate displacement is derived from the inverse Hankel transform:

$$W(r) = \int_0^\infty \hat{W}(\gamma) \gamma J_0(\gamma r) d\gamma, \tag{13.74}$$

which yields, finally:

$$W(r) = \frac{F_0}{2\pi D} \int_0^\infty \frac{J_0(\gamma r)}{\gamma^4 - k_B^4} \gamma d\gamma. \tag{13.75}$$

The integral in (13.75) yields: (see [21, 31, 40]):

$$W(r) = \frac{j F_0}{8\omega \sqrt{\rho_p h D}} \left[H_0^{(2)}(k_B r) - \frac{2j}{\pi} K_0(k_B r) \right], \tag{13.76}$$

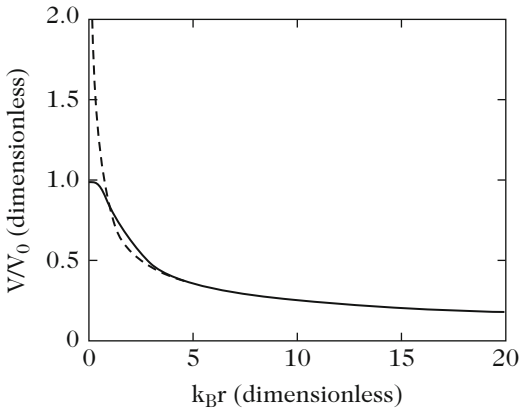

Fig. 13.14 Point-excited infinite plate at constant frequency. Modulus of the plate velocity V as a function of the distance from the excitation point. *Dotted line*: approximate solution, valid for $k_B r > 4$. $V_0 = |j\omega W(0)|$

where $H_0^{(2)}$ is the zero-order Hankel function of the second kind defined by:

$$H_0^{(2)}(x) = J_0(x) - jY_0(x). \tag{13.77}$$

In this expression, $Y_0(x)$ is the zero-order Bessel function of the second kind, and $K_0(x)$ is the modified zero-order Hankel function [1].

Figure 13.14 shows the modulus $V = j\omega W$ of the plate velocity as a function of the normalized distance $k_B r$, and the approximate solution:

$$V \simeq \frac{F_0}{\sqrt{\rho_p h D}} \sqrt{\frac{2}{\pi k_B r}}, \tag{13.78}$$

which is valid for $k_B r > 4$.

At the excitation point, the term between square brackets in Eq. (13.76) is equal to one. The driving impedance is defined by the fraction:

$$Z_p(0) = \frac{F_0}{j\omega W(0)} = 8\sqrt{\rho_p h D} = 4h^2 \sqrt{\frac{\rho_p E}{3(1-\nu^2)}}. \tag{13.79}$$

The remarkable result here is that this impedance is real and does not depend on frequency. It depends on the thickness and on the material properties of the plate, only. Notice, however, that this result is only true for a thin plate (Kirchhoff–Love model). The driving admittance (or mobility) is given by $Y_p(0) = 1/Z_p(0)$.

The expression (13.79) can be used for validating measurements of driving impedance (or admittance) of finite damped isotropic thin plates, in the high frequency range. In general, the losses increase with frequency, so that the returning waves reflected at the boundaries can be neglected. Equation (13.79) can then be viewed as an asymptotic limit. Benefit will be taken from this expression at the end

of the chapter for defining a "merit index" for stringed instruments, whose interest is to help in the selection of appropriate materials for the soundboard.

A similar expression can be found for anisotropic plates [4, 7]. For an orthotropic plate, for example, the following approximation is usually admitted:

$$Z_p(0) \simeq 4h^2 \sqrt{\frac{\rho_p [E_1 E_2]^{1/2}}{3(1-\nu^2)}}, \tag{13.80}$$

where E_1 is the Young's modulus in the direction of the fibers, and E_2 the modulus perpendicular to the fibers [19].[8]

Taking further the structural losses into account, then the Young's modulus becomes complex of the form $E[1 + j\eta(\omega)]$. For most materials used in instrument making, η increases with frequency. As a consequence, the modulus $|Z(\omega)|$ increases and the admittance $|Y(\omega)|$ decreases with frequency.

Most soundboards of musical instruments are not homogeneous, due to the presence of ribs glued on one side. The driving-point mobility of isotropic plates reinforced by periodic ribs was investigated by Nightingale and Bosmans [28]. One conclusion of this study is that the measured mobility greatly depends on the distance between the driving point and the closest rib, as long as this distance is small compared to the flexural wavelength. For a driving-point close to a rib, the measured real part of $Y_p(0)$ corresponds to the mobility of the rib (beam). As soon as the rib-driving-point distance becomes larger than the wavelength, then the measured mobility tends to the theoretical value obtained for a plate with constant thickness. These results are of interest for understanding and interpreting the driving-point mobility measurements performed on a piano, for example.

Impulse Excitation

For a given load $q(r, t)$ in the time domain, the governing equation for the plate displacement $w(r, t)$ is

$$D\left(\frac{\partial^2}{\partial r^2} + \frac{1}{r}\frac{\partial}{\partial r}\right)^2 w + \rho_p h \frac{\partial^2 w}{\partial t^2} = q(r, t). \tag{13.81}$$

Let us assume that the plate is initially at rest ($w(r, 0) = \dot{w}(r, 0) = 0$). Denoting $b^2 = D/\rho_p h$, the particular case of an impulse excitation of the form:

(continued)

[8] In this expression, it is assumed that the Poisson's coefficients are identical in both directions.

$$q(r,t) = 8b\rho_p h f(r)\delta(t), \quad \text{where} \quad \int_0^\infty 2\pi r f(r) dr = 1 \quad \text{so that} \quad f(r) = \frac{\delta(r)}{2\pi r}. \tag{13.82}$$

is examined. The full calculation was done by Graff [17]. The following solution is obtained

$$w(r,t) = \frac{2}{\pi}\int_0^t \frac{u}{t-u} \sin\left[\frac{r^2}{4b(t-u)}\right] du. \tag{13.83}$$

The displacement can be rewritten in the form:

$$w(r,t) = 1 - \frac{2}{\pi}\mathrm{Si}\left(\frac{r^2}{4bt}\right) \quad \text{where} \quad \mathrm{Si}(x) = \int_0^x \frac{\sin z}{z} dz, \tag{13.84}$$

and where $\mathrm{Si}(x)$ denotes the *sine integral* function.

Figure 13.15 shows the motion of the plate at a given fixed time t_0, and the temporal evolution of one particular point. It shows, among other things, the presence of a precursor where the most rapid oscillations arrive first, due to the properties of the dispersion equation.

13.3.7.2 Fluid-Loaded Plate

The purpose of this paragraph is to evaluate the influence of the fluid (acoustic field) on the plate for a harmonic excitation on a single point. The results presented below should be compared to those obtained for a plate in vacuo (see Sect. 13.3.7.1).

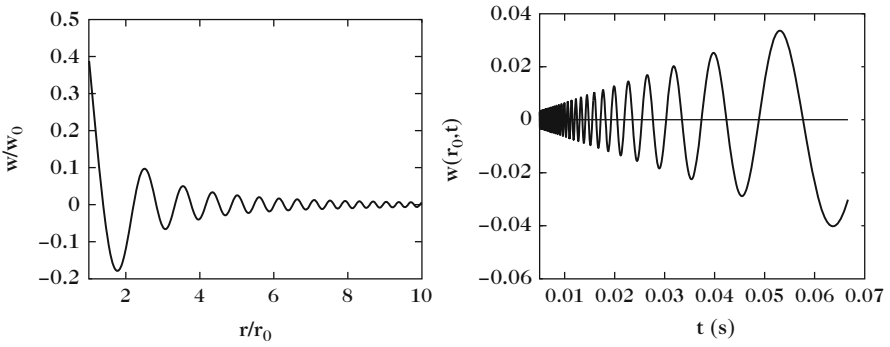

Fig. 13.15 Impulse excitation of a plate. (*Left*) Global motion of the plate at a fixed time $t = t_0$. (*Right*) Temporal evolution of the plate displacement at a given point $r = r_0$

Taking now the radiated pressure exerted on both sides of the plate into account, the equation of motion is modified as follows:

$$D\left(\frac{d^2}{dr^2}+\frac{1}{r}\frac{d}{dr}\right)^2 W-\rho_p h\omega^2 W=\frac{F_0\delta(r)}{2\pi r}-P(r,z=0^+)+P(r,z=0^-), \tag{13.85}$$

where the z-axis is perpendicular to the plate. The plate is located in the plane $z=0$. As in Sect. 13.3.7.1, this equation can be solved by means of the Hankel transform [17, 40]. Denoting $\hat{P}(\gamma,0)$ the Hankel transform of the pressure, and $\hat{W}(\gamma)$ the transform of the displacement, we get

$$D\left(\gamma^4-k_B^4\right)\hat{W}(\gamma)=-\hat{P}(\gamma,0^+)+\hat{P}(\gamma,0^-)+\frac{F_0}{2\pi}. \tag{13.86}$$

Noticing that the first term in the left-hand side of Eq. (13.86) has the dimension of a pressure, the Hankel transform of the driving-point impedance of the plate can be defined as:

$$\hat{Z}_p(\gamma)=\frac{D\left(\gamma^4-k_B^4\right)}{j\omega}. \tag{13.87}$$

According to (13.62), the pressure is written:

$$\hat{P}(\gamma,0)=j\omega\hat{Z}_a(\gamma)\hat{W}\quad\text{with}\quad\hat{Z}_a(\gamma)=\rho\frac{\omega}{\sqrt{k^2-\gamma^2}}. \tag{13.88}$$

Equation (13.86) becomes

$$j\omega\hat{W}(\gamma)=\frac{F_0}{2\pi}\frac{1}{\hat{Z}_p(\gamma)+2\hat{Z}_a(\gamma)}. \tag{13.89}$$

Through inverse Hankel transform, the displacement of the plate is derived

$$W(r)=\frac{F_0}{j2\pi\omega}\int_0^\infty\frac{\gamma J_0(\gamma r)}{\hat{Z}_p(\gamma)+2\hat{Z}_a(\gamma)}d\gamma. \tag{13.90}$$

This last equation can be solved using contour integration in the complex plane, or numerically [21]. The Hankel transform of the radiated pressure is obtained through the Helmholtz equation combined with the continuity of the normal velocities on the plate, as in Sect. 13.3.4. These derivations are not detailed further here. Finally, we obtain

$$\text{for } z>0\quad\hat{P}(\gamma,z)=j\omega\hat{Z}_a(\gamma)\hat{W}(\gamma)e^{-jz\sqrt{k^2-\gamma^2}}, \tag{13.91}$$

which yields, in turn:

$$P(r,z) = \frac{F_0}{2\pi}\int_0^\infty \frac{\hat{Z}_a(\gamma)}{\hat{Z}_p(\gamma)+\hat{Z}_a(\gamma)}\gamma J_0(\gamma r)e^{-jz\sqrt{k^2-\gamma^2}}d\gamma. \tag{13.92}$$

The far field pressure $P(r,z)$ can be derived by using the method of stationary phase [21]. With the change of coordinates $r = R\sin\theta$ and $z = R\cos\theta$, the following expression is obtained for the half-plane $z > 0$, and for $kR \gg 1$:

$$P(R,\theta) = \frac{jkF_0e^{-jkR}}{2\pi R}\frac{\cos\theta}{1+jkh\frac{\rho_p}{\rho}\cos\theta\left[1-\frac{\omega^2}{\omega_c^2}\sin^4\theta\right]}. \tag{13.93}$$

Discussion

A few remarks can be made with regard to the expression of the far field pressure calculated in (13.93):

- In the direction perpendicular to the plate ($\theta = 0$), the pressure reduces to:

$$P(R,0) = \frac{jkF_0e^{-jkR}}{2\pi R}\frac{1}{1+jkh\frac{\rho_p}{\rho}}. \tag{13.94}$$

  This result shows that, due to the loading, the pressure is multiplied by a correcting factor which depends on the surface density $\rho_p h$ of the plate only (in particular, this factor does not depend on the plate rigidity D). In other words, *the far field pressure of a plate is similar to the one radiated by a membrane with the same surface density*.
- In addition, if the plate can be considered as sufficiently thin or, equivalently, that the frequency is sufficiently small so that one can assume that $kh\frac{\rho_p}{\rho} \ll 1$, then we have

$$P(R,0)_{\text{lim}} \approx \frac{jkF_0e^{-jkR}}{2\pi R}. \tag{13.95}$$

  Under these assumptions, it can be seen that the pressure is equivalent to the one radiated by a point source with imposed force F_0.
- For frequencies below the critical frequency, $P(R,0)$ is the maximum of the pressure. In contrast, in the supersonic range, pressure maxima can exist with larger amplitudes than $P(R,0)$ in some particular directions θ_c defined by the condition:

$$\theta_c = \sin^{-1}\left(\frac{\omega_c}{\omega}\right)^{1/2}. \tag{13.96}$$

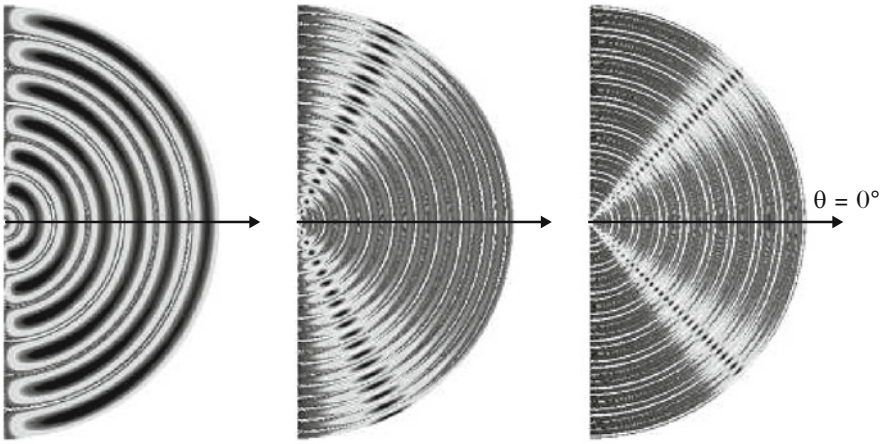

Fig. 13.16 Pressure field radiated by a thin isotropic plate loaded by the air. (*Left*) $f = 0.4f_c$; (*Center*) $f = 1.2f_c$; (*Right*) $f = 2.0f_c$. The horizontal arrow is perpendicular to the plate plane and corresponds to the direction $\theta = 0$. The *light-gray* zones (for $f > f_c$, *middle and right* figures) indicate the directions of maximum pressure. For $f < f_c$ (*left* figure), there are no preferential directions, and the directivity pattern is close to the radiation pattern of a dipole [31]

Figure 13.16 shows the sound pressure radiated by an isotropic plate, for different frequencies (below and above the critical frequency of the plate).

- In practice, the magnitude of the pressure is limited by the internal damping inside the plate. This is particularly true in the supersonic range, above the critical frequency.

13.4 Radiation from Finite Plates

In a number of past studies, it has been shown that finite plates are relevant to account for the radiation of stringed instruments, at least to a first approximation (see Fig. 13.17) [11]. In fact, it is plain that guitar, violin or piano soundboards cannot be strictly modeled as plates. Other components such as the ribs, the sound holes and the bridge, for example, and geometrical factors such as the curvature contribute to add perturbations in the model [15, 16]. However, the finite plate model is a good reference for presenting the basic principles that govern the structural acoustics of stringed and percussive instruments. It also yields interesting reference solutions which might be helpful in case of numerical approach. This explains why the radiation of finite plates is presented in detail below. The application of the results to real instruments, as well as the study of some particular modifying features will be examined later in this section.

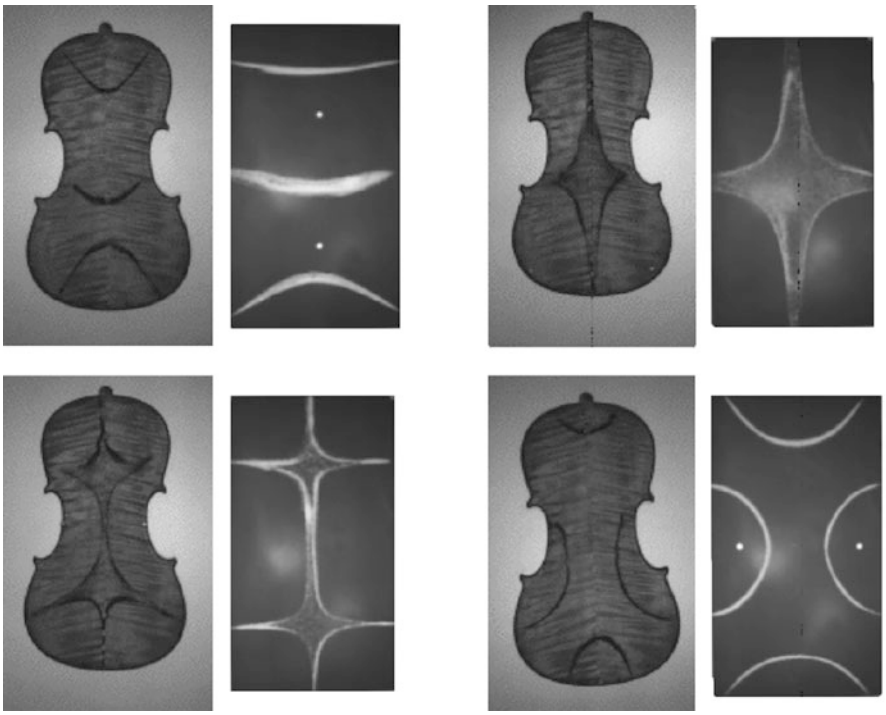

Fig. 13.17 Relevance of the plate model in the case of violin plates. A few low-order modal shapes of violin back plates are presented. These shapes are very similar to those of a metallic plate of comparable dimensions. The Chladni patterns were obtained in a similar way as for the guitar modes in Chap. 3. After [41]

13.4.1 Spatial Fourier Transform

The purpose of this section is to calculate the acoustic field radiated by a thin rectangular isotropic vibrating plate, simply supported along its edges. The vibratory properties of such a plate were presented in Chap. 3. It is assumed that the plate is inserted in an infinite rigid baffle, so that the Rayleigh formula presented in Chap. 12 can be used. It is also assumed that the observation point is located at a sufficiently large distance from the plate, in order to take advantage of the Fraunhofer approximation defined in the same chapter. The geometry of the problem is shown in Fig. 13.18. W denotes the flexural displacement of the plate. Cartesian coordinates are used. All derivations are made for an harmonic excitation of the plate with frequency ω. The radiated pressure is written:

$$P(\mathbf{r},\omega) = -\frac{\omega^2\rho}{2\pi r}\int_S W(x',y',\omega)e^{-jk|\mathbf{r}-\mathbf{r}'|}dS_{(\mathbf{r}')}, \tag{13.97}$$

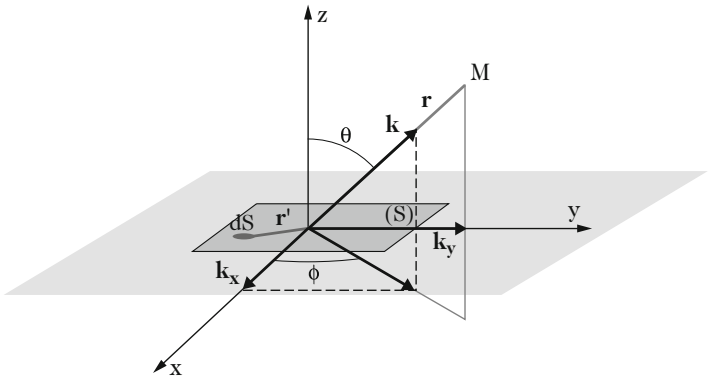

Fig. 13.18 Geometry used for calculating the radiation of a rectangular plate inserted in an infinite baffle. $k_x = k \sin\theta \cos\Phi$ and $k_y = k \sin\theta \sin\Phi$

which can be written, equivalently:

$$P(r, \theta, \Phi, \omega) = -\frac{\omega^2 \rho}{2\pi r} e^{-jkr} \int_S W(x', y', \omega) e^{+j(k_x x' + k_y y')} dx' dy', \tag{13.98}$$

with $k_x = k \sin\theta \cos\Phi$ and $k_y = k \sin\theta \sin\Phi$. A fundamental result is found in Eq. (13.98): if the distance between the observation point and the plate is large compared to the dimensions of the plate, then the radiated pressure is proportional to the *spatial Fourier transform* of the plate displacement:

$$P(r, \theta, \Phi, \omega) = -\frac{\omega^2 \rho}{2\pi r} e^{-jkr} \tilde{W}(k_x, k_y, \omega). \tag{13.99}$$

This property can be viewed as a generalization of the previously obtained result for the plane piston in Chap. 12.

13.4.2 Contribution of the Vibrating Modes to the Radiated Pressure

In what follows, the internal damping in the plate material and the reaction of the acoustic field against the plate are left temporarily aside. The displacement field if the plate is projected onto the its eigenmodes basis:

$$W(x, y, \omega) = \sum_{m=1}^{\infty} \sum_{n=1}^{\infty} A_{mn}(\omega) \phi_{mn}(x, y). \tag{13.100}$$

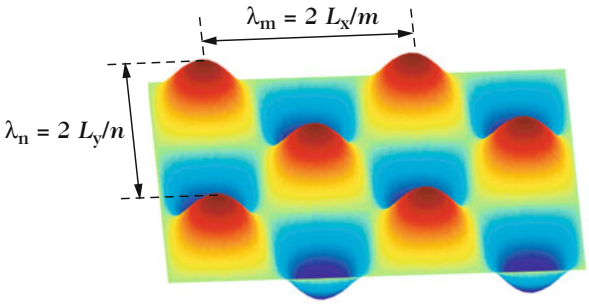

Fig. 13.19 Modal shape of a simply supported rectangular plate for ($m = 4, n = 3$). The respective quantities λ_m and λ_n determine the spatial periodicity along the x and y axis

For a simply supported plate of length L_x and width L_y, the eigenmodes are written:

$$\phi_{mn}(x,y) = \frac{2}{\sqrt{L_x L_y}} \sin\left(\frac{m\pi}{L_x}x\right) \sin\left(\frac{n\pi}{L_y}y\right) \tag{13.101}$$

where the normalization factor has been selected so that $\int_S \phi_{mn}^2 dS = 1$. An example of modal shape is shown in Fig. 13.19.

The contribution P_{mn} of the mode (m,n) to the total sound pressure is defined by:

$$P_{mn}(r,\theta,\Phi) = -\frac{\omega^2\rho}{2\pi r} e^{-jkr} A_{mn}\, \tilde{\phi}_{mn}(k_x,k_y,\omega). \tag{13.102}$$

Thus, the problem reduces to calculating the spatial Fourier transform of the modal shape $\phi_{mn}(x,y)$. This calculation is rather tedious by hand, though it becomes straightforward with currently available numerical tools. The result in the simple case presented here is written [40]:

$$P_{mn}(r,\theta,\Phi,\omega) = -\frac{\omega^2\rho}{r} e^{-jkr} A_{mn}\, \pi mn \sqrt{L_x L_y} \left[\frac{(-1)^m e^{+jk_x L_x} - 1}{(k_x L_x)^2 - m^2\pi^2}\right] \left[\frac{(-1)^n e^{+jk_y L_y} - 1}{(k_y L_y)^2 - n^2\pi^2}\right]. \tag{13.103}$$

For a given angular frequency ω, Eq. (13.103) shows that particular directions exist in space where the modal contribution P_{mn} is high. These directions fulfill the conditions $k_x L_x \approx m\pi$ and $k_y L_y \approx n\pi$.[9] The corresponding directions θ_{mn} and Φ_{mn} (also called *directions of spatial coincidence*) are given by:

[9]These values correspond to the maxima of the functions $\left|\frac{(-1)^m e^{+jk_x L_x}-1}{(k_x L_x)^2 - m^2\pi^2}\right|$ and $\left|\frac{(-1)^n e^{+jk_y L_y}-1}{(k_y L_y)^2 - n^2\pi^2}\right|$. Except for the lowest values of m and n, these maxima are close to $m\pi$ and $n\pi$.

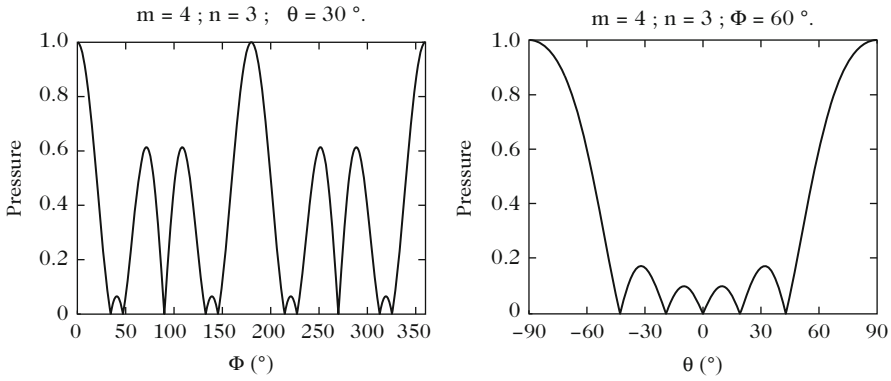

Fig. 13.20 Examples of spatial coincidence for the plate mode $m = 4$; $n = 3$, at a frequency of 1 kHz. $L_x = 1\,\text{m}$; $L_y = 0.6\,\text{m}$

$$k \sin\theta_{mn} \cos\Phi_{mn} = k_m = \frac{m\pi}{L_x} \quad \text{and} \quad k \sin\theta_{mn} \sin\Phi_{mn} = k_n = \frac{n\pi}{L_y}. \tag{13.104}$$

Examples of spatial coincidence are shown in Fig. 13.20. In addition, the pressure components P_{mn} are subjected to *frequency coincidence* through the expression of the modal amplitudes A_{mn}. In Chap. 3, it was shown that, for a plate excited with a force F at point (x_0, y_0), this amplitude is

$$A_{mn} = \frac{F}{\rho_p h} \frac{\phi_{mn}(x_0, y_0)}{\omega_{mn}^2 - \omega^2 + 2j\zeta_{mn}\omega\omega_{mn}}, \tag{13.105}$$

where the ω_{mn} are the eigenfrequencies of the plate, and ζ_{mn} the modal damping factors which are assumed to be small compared to unity. For simply supported rectangular plates, the eigenfrequencies are given by:

$$\omega_{mn} = \sqrt{\frac{D}{\rho_p h}} \left[\frac{m^2\pi^2}{L_x^2} + \frac{n^2\pi^2}{L_y^2} \right] = \sqrt{\frac{D}{\rho_p h}} \left[k_m^2 + k_n^2 \right]. \tag{13.106}$$

In summary, situations may occur where a plate mode is vibrating with high amplitude (frequency coincidence), although the corresponding sound pressure is low, if the condition of spatial coincidence is not fulfilled. In other words, resonant modes might not be always efficient in terms of radiated power. Different particular cases are now examined.

13.4.2.1 Radiated Sound Pressure

- For large wavelengths, i.e., for $k \to 0$ in (13.103), the pressure becomes

$$P_{mn} \to B_{mn} \frac{e^{-jkr}}{r}, \tag{13.107}$$

where B_{mn} depends only on ω. This means that the directivity index is constant. The pressure is similar to the one radiated by a pulsating sphere.

- In Eq. (13.104), one can see that the coincidence angles exist only if $k_n < k$ and $k_m < k$, since the sine and cosine functions are bounded by one. In terms of wavelengths, this means that the acoustic wavelength λ has to be smaller than $\lambda_m = 2L_x/m$ and $\lambda_n = 2L_y/n$ (see Fig. 13.19). For subsequent discussion, it is convenient to introduce the *structural* wavenumber $k_{mn} = \sqrt{k_m^2 + k_n^2}$. From Eq. (13.104), the directions θ_{mn} are given by:

$$\theta_{mn} = \sin^{-1} \frac{k_{mn}}{k}. \tag{13.108}$$

This shows that θ_{mn} exist under the additional condition $k_{mn} < k$, i.e., when the acoustic wavelength is smaller than the elastic wavelength in the plate. This is a generalization of the result obtained for an infinite plate. This condition can occur only for frequencies beyond the critical frequency defined in (13.51). It can be also checked that:

$$\Phi_{mn} = \tan^{-1} \frac{k_n}{k_m}. \tag{13.109}$$

Examples of two cases ($k_n < k$ with $k_m < k$ and $k_{mn} > k$, part; $k_n < k$ with $k_m < k$ and $k_{mn} < k$) are shown in Fig. 13.21.

- Some intermediate configurations also exist, corresponding to the cases where $k_n < k$ and $k_m > k$, or $k_n > k$ and $k_m < k$. In these cases, there are no maxima for Φ. However, one can observe maxima for the angles θ which fulfill the conditions:

$$\begin{cases} \text{for } k_n < k \text{ and } k_m > k \ : \ \theta_n = \sin^{-1}\left(\dfrac{k_n}{k\cos\Phi}\right), \\ \text{for } k_m < k \text{ and } k_n > k \ : \ \theta_m = \sin^{-1}\left(\dfrac{k_m}{k\cos\Phi}\right). \end{cases} \tag{13.110}$$

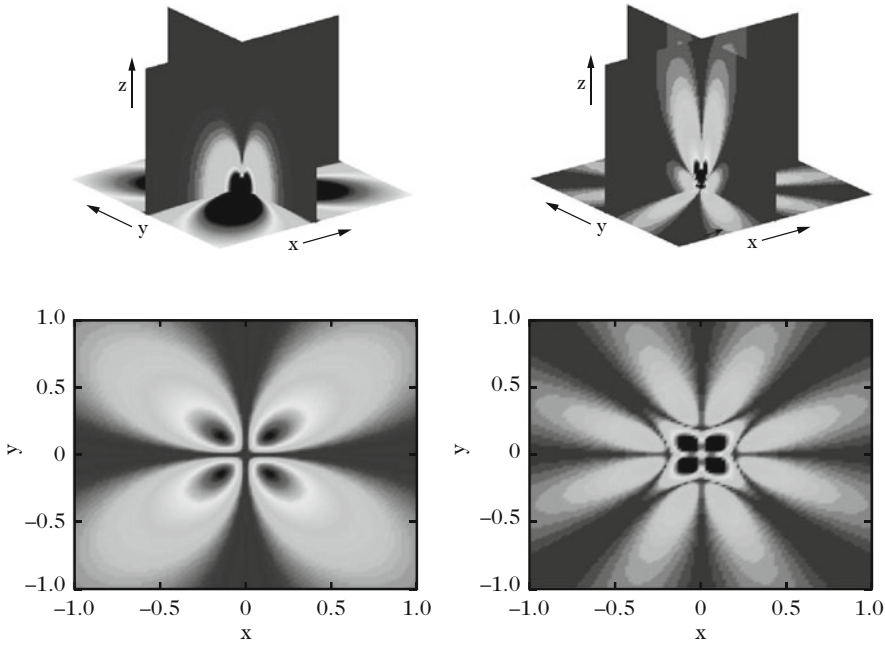

Fig. 13.21 Pressure radiated by some particular modes (m, n) of a simply supported rectangular plate. (*Left*) $k_n < k$ and $k_m < k$ and $k_{mn} > k$: the pressure vanishes in some directions (Φ) of the *horizontal* plane, but not in the *vertical* plane (θ). (*Right*) $k_n < k$ and $k_m < k$ and $k_{mn} < k$: the pressure vanishes for some particular directions in *both* the *horizontal* and *vertical* planes

13.4.2.2 Intermodal Radiation Impedances

Using the spatial Fourier transform of the displacement, the radiated pressure can be written alternatively [26]:

$$P(x, y, z, \omega)) = j\frac{\rho\omega^2}{4\pi^2}\int_{-\infty}^{+\infty}\int_{-\infty}^{+\infty}\frac{\tilde{W}(k_x, k_y)}{k_z}e^{-jk_z z}e^{j(k_x x + + k_y y)}\,dk_x dk_y,$$

$$\text{where} \quad k_z = \sqrt{k^2 - k_x^2 - k_y^2}. \tag{13.111}$$

Based on the modal expansion of the displacement (13.100), one can derive the surface pressure (in the plate plane $z = 0$):

$$P(x, y, 0, \omega) = \sum_{m,n}\sum_{r,s} j\omega A_{mn}(\omega)Z_{mnrs}(\omega)\phi_{rs}(x, y), \tag{13.112}$$

(continued)

where the Z_{mnrs} are the intermodal radiation impedance given by:

$$Z_{mnrs}(\omega) = \frac{\rho\omega}{4\pi^2}\int_{-\infty}^{+\infty}\int_{-\infty}^{+\infty}\tilde{\phi}_{mn}(k_x,k_y)\,\tilde{\phi}_{rs}(-k_x,-k_y)\,dk_x dk_y. \qquad (13.113)$$

The real part of the Z_{mnrs} corresponds to the dissipated acoustic power. The imaginary part accounts for the fluid loading. In free field, the imaginary part is positive and, in turn, the eigenfrequencies of the plate decrease compared to the in vacuo case. These expressions generalize the result obtained in Chap. 12 in the case of the plane piston. For "light" fluids, the reactive effects are often negligible, except for light and flexible structures (see Chap. 14).

In this section the comparison between acoustic and elastic wavenumber presented in Sect. 13.3 for infinite plates has been generalized to finite plates. The main difference between both cases is due to the fact that the elastic wavenumber can take only discrete values for finite plates. In addition, as a consequence of the spatial periodicity of the vibratory field on the plate, the magnitude of the pressure field is subjected to strong variations with regard to the direction of propagation in the air in the supersonic range. These directions vary a lot with the geometry of the mode. During normal playing of an instrument, different modes are excited successively. Consequently, the directivity of the instrument changes continuously.

13.4.3 Radiated Acoustic Power

13.4.3.1 Single Modal Contribution

The radiated acoustic power is calculated by integration of the flow of the acoustic intensity vector through a closed surface at a given distance r from the plate. The calculation is simple for a spherical surface in the far field. We get

$$\langle \mathscr{P}_a|_{mn}(\omega)\rangle = \frac{1}{2\rho c}\int_0^{2\pi}\int_0^{\pi/2}|P_{mn}(r,\theta,\Phi,\omega)|^2\,r^2\sin\theta\,d\theta\,d\Phi, \qquad (13.114)$$

where P_{mn} is given by (13.103). As for the infinite plate, the radiation efficiency is defined by the ratio:

$$\sigma_{mn}(\omega) = \frac{\langle \mathscr{P}_a|_{mn}(\omega)\rangle}{\frac{1}{2}\rho c L_x L_y \langle|\dot{W}_{mn}|^2\rangle}, \qquad (13.115)$$

where $\langle|\dot{W}_{mn}|^2\rangle$ is the mean quadratic velocity defined as:

$$\langle |\dot{W}_{mn}|^2 \rangle = \frac{1}{L_x L_y} \int_0^{L_x} \int_0^{L_y} |\dot{W}_{mn}(x, y, \omega)|^2 \, dxdy. \tag{13.116}$$

The efficiency σ_{mn} is proportional to the radiation resistance of the mode mn:

$$R_{amn}(\omega) = \frac{\langle \mathscr{P}_a|_{mn}(\omega) \rangle}{\frac{1}{2}\langle |\dot{W}_{mn}|^2 \rangle} = \rho c L_x L_y \sigma_{mn}(\omega). \tag{13.117}$$

In the particular case of the simply supported rectangular plate, the calculation based on (13.103) leads to the expression:

$$\sigma_{mn}(\omega) = \frac{16k^2 L_x L_y}{\pi^6 m^2 n^2} \int_0^{2\pi} \int_0^{\pi/2} \left(\frac{\left\{ \begin{matrix} \cos \\ \sin \end{matrix} \right\} \frac{k_x L_x}{2} \left\{ \begin{matrix} \cos \\ \sin \end{matrix} \right\} \frac{k_y L_y}{2}}{\left[\left(\frac{k_x L_x}{m\pi} \right)^2 - 1 \right] \left[\left(\frac{k_y L_y}{m\pi} \right)^2 - 1 \right]} \right)^2 \sin\theta d\theta d\phi. \tag{13.118}$$

In (13.118), the *cosine* function is used for odd values of m (resp. n), and the *sine* function is used for even values of these indices.

Figure 13.22 shows some examples of radiation efficiencies of a rectangular plate [38], as a function of the ratio:

$$\gamma = k/k_{mn} = \frac{k}{\sqrt{\left(\frac{m\pi}{L_x} \right)^2 + \left(\frac{n\pi}{L_y} \right)^2}}$$

For $k > k_{mn}$, the modal efficiencies tend to unity, as for the limiting case of the infinite plate.

For $k < k_{mn}$, σ_{mn} is weak but nonzero (as it was the case for infinite plates: see Fig. 13.11). Close examination shows that, depending on the values taken by m and n, two different situations may occur, depending whether the plate radiates by the edges or by the corners, as shown in the next section.

13.4.3.2 Edge and Corner Radiation

Figure 13.23 (left) shows a typical situation of corner radiation. This corresponds to the vibration of the plate at a frequency ω so that the following conditions are fulfilled:

$$k < k_{mn}, \; k_m = \frac{m\pi}{L_x} > k \quad \text{and} \quad k_n = \frac{n\pi}{L_y} > k.$$

In the case presented in Fig. 13.23, the contributions of the elementary "dipoles" on the plate to the radiated power are close to zero (see Chap. 12), except for the

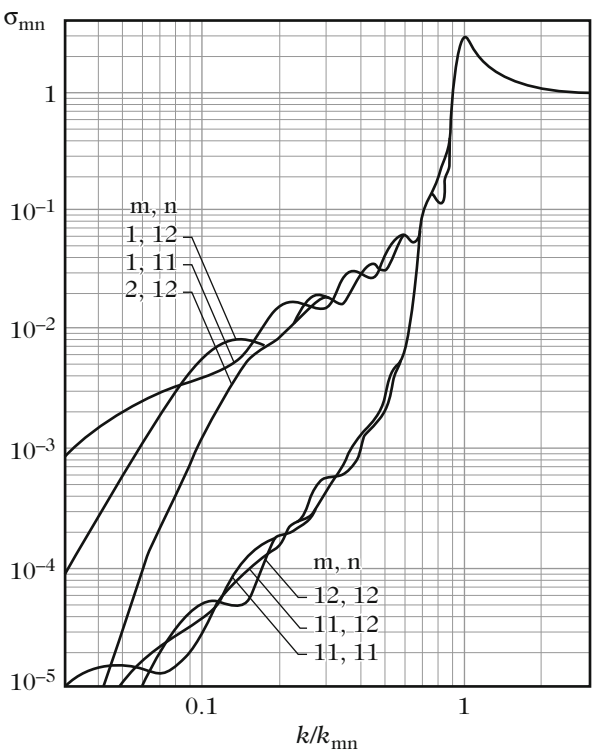

Fig. 13.22 Examples of modal radiation efficiencies σ_{mn} as a function of $\gamma = k/k_{mn}$ for a rectangular plate, after Wallace [38]. For $\gamma < 1$, the modes $(1, 12)$, $(1, 11)$, and $(2, 12)$ are radiating only by the edges, whereas the modes $(12, 12)$ $(11, 11)$, and $(11, 12)$ are radiating by the corners

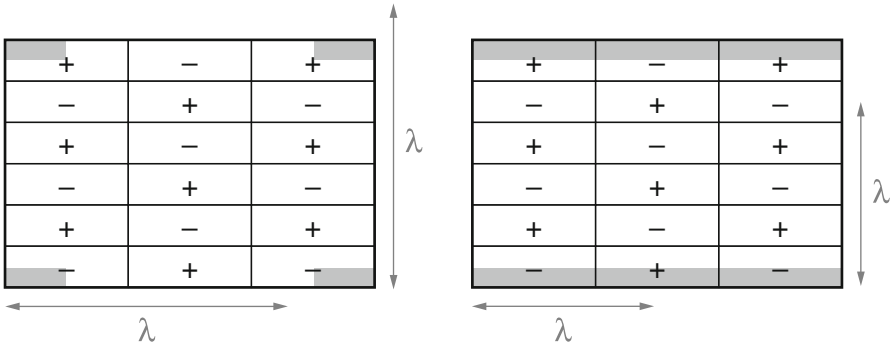

Fig. 13.23 (*Left*) Corner radiation of a rectangular plate: $\lambda > \lambda_m$ $(k < k_m)$ and $\lambda > \lambda_n$ $(k < k_n)$. (*Right*) Edge radiation of a rectangular plate: $\lambda < \lambda_m$ $(k > k_m)$ and $\lambda > \lambda_n$ $(k < k_n)$. Only the *gray* zones are efficient in terms of radiation. The radiation efficiency is close to zero in the other parts of the plate, since the distance between the centers of the zones (with opposite signs) is less than one wavelength. This is a consequence of the dipole properties demonstrated in Chap. 12

four zones at the corners since, in this latter case, the distance between the zones is larger than an acoustic wavelength. Similarly, the edge radiation corresponds to the conditions:

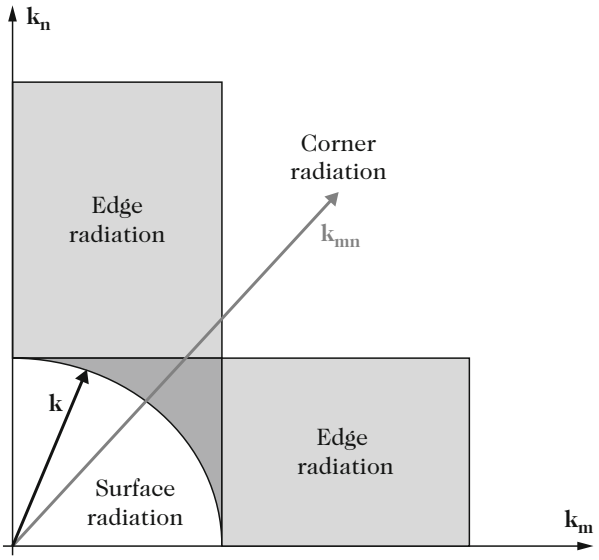

Fig. 13.24 Surface, edge, and corner radiation

$$k < k_{mn} \quad \text{and}$$
$$\left(k_m = \frac{m\pi}{L_x} < k \quad \text{and} \quad k_n = \frac{n\pi}{L_y} > k\right) \quad \text{or} \quad \left(k_m = \frac{m\pi}{L_x} > k \quad \text{and} \quad k_n = \frac{n\pi}{L_y} < k\right).$$

Here a similar situation as for the corner radiation is obtained, along the y axis only. The radiation efficiency only results from the gray zones situated close to the edges in $y = 0$ and $y = L_y$. In the case shown in Fig. 13.23, the acoustic wavelength λ is smaller than the spatial periodicity $\lambda_m = 2L_x/m$ of the mode along the x axis and, as a consequence, the different contributions to the radiation do not cancel each other in this direction.

A summary of all possible situations is shown in Fig. 13.24. In addition to the cases of edge and corner radiation, the third case corresponds to the conditions

$$k_{mn} < k, \; k_m = \frac{m\pi}{L_x} < k \quad \text{and} \quad k_n = \frac{n\pi}{L_y} < k,$$

where the whole surface contributes to the radiation. The corresponding zone in the k-plane is inside the quarter circle of radius k.

The dark gray zone located between the quarter circle of radius k and the square of side k corresponds to particular edge modes where the periphery of the whole surface contributes to the radiation efficiently. The width of the radiating zone increases progressively as the operating point comes closer to the quarter circle (see Fig. 13.25).

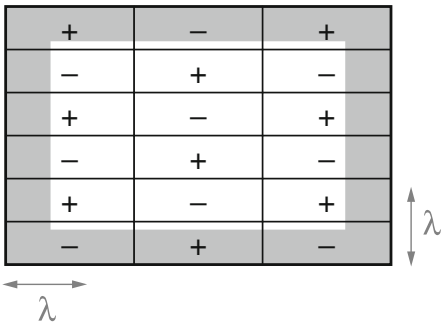

Fig. 13.25 Edge radiation in x and y directions simultaneously, or "incomplete" surface modes. $\lambda < \lambda_m$ ($k > k_m$) and $\lambda < \lambda_n$ ($k > k_n$) and $k < k_{mn}$

In summary, surface modes are the most efficient in terms of radiation, followed by the edge, and then by the corner modes.

13.4.3.3 Forced Excitation of a Rectangular Plate

In the previous paragraph, the different possible situations governing the radiation of finite rectangular plates were presented. This allows us now to address the case of the forced excitation of a plate at a given frequency ω. Such situation is close to the real case of a guitar or piano string excited by a particular frequency component of the string's vibration. In fact, the decay time of plucked and struck strings is usually much larger than the one of the body, and thus, to a first approximation, the string excitation can be considered as "forced."

Subsonic Case

Figure 13.26, inspired by Williams [40] shows an example where the excitation frequency is less than the critical frequency of the plate (*subsonic* case), which corresponds to the condition $k_B > k$ in terms of wavenumber (see Fig. 13.6). In this figure, the bullets "•" indicate the eigenmodes of the plate in terms of wavenumber.

- For a given frequency ω, the geometric locus of k_B is a "structural" quarter circle with radius larger than the "acoustic" quarter circle of radius $k = \omega/c$.
- Considering the modal vibration amplitudes A_{mn} [see Eq. (13.105)], one can derive that all modes close to the "structural" quarter circle are likely to be excited, which corresponds to the condition $\omega \approx \omega_{mn}$. This region of modal excitation is shown as a gray zone in Fig. 13.26. The width of this zone increases with the modal damping, which means that the resonance peaks are wider.
- As a consequence of the spreading of this zone, three family of modes can be excited by the forcing frequency ω: edge, corner, and surface modes. The surface modes (which are the most efficient in terms of radiation) correspond to the

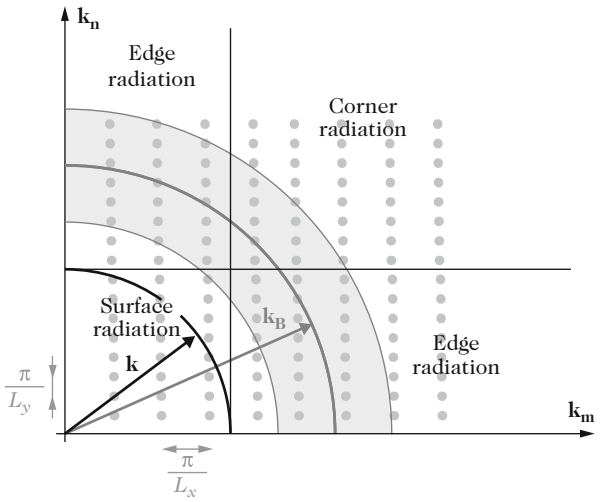

Fig. 13.26 Subsonic forced excitation of a rectangular plate. After Williams [40]

smallest values of the wavenumber in the zone (m and n such as $k_{mn} < k$). As a result, even if the vibratory magnitude A_{mn} of these surface modes is smaller than the one of the corner and edge mode at this forcing frequency, because of the distance between ω_{mn} and ω, their acoustical efficiency is higher since k_{mn} are closer to k.

For the instruments for which a plate radiation model is pertinent (piano or guitar soundboard, for example), the immediate practical consequence of the property presented above is that, in the subsonic case, the lowest modes may contribute to the radiation significantly, even if the excitation frequencies of the strings are relatively well apart from the corresponding modal frequencies of these modes.

Supersonic Case

In view of the usual order of magnitude for the soundboard materials and geometry used in stringed instruments, the elasto-acoustic interaction can be considered as subsonic below 1–5 kHz, depending on the practical case. As a consequence, almost all fundamental frequencies belong to this interval. However, it is not the case for the higher partials of the notes, which can have frequencies up to 20 kHz (and even more, in the case of the cembalo, for example). Thus, for these higher partials, the *supersonic case* also has to be examined.

Both the structural and acoustic wavelengths decrease as the forcing frequency increases. Because of the dispersion properties of the plate, the acoustic wavelength decreases faster, and thus, above the so-called critical frequency (see Sect. 13.3), the acoustic wavelength becomes smaller than the structural one. It has been shown

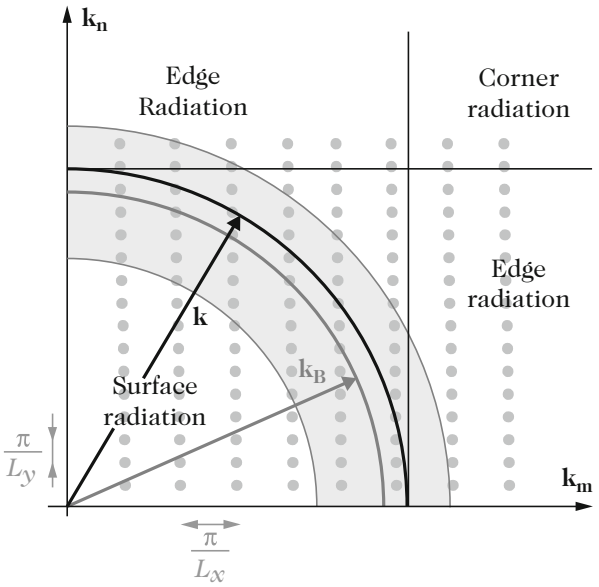

Fig. 13.27 Forced supersonic excitation of a rectangular plate

previously in this chapter that we are then in the case of a supersonic regime where the complete surface of the plate radiates efficiently. In terms of wavenumber, this case is shown in Fig. 13.27. The modes inside the gray ring in the vicinity of the quarter circle of radius k_B are together highly resonating (ω close to ω_{mn}) and radiating modes ($k_{mn} < k$).

The radiation efficiency defined in (13.115) is close to unity for all surface modes (see Fig. 13.22). recall that this quantity is normalized by the quadratic mean velocity $\langle|\dot{W}_{mn}|^2\rangle$, and thus, in turn, by the square of the modal amplitude A_{mn}. For stringed instruments, these amplitudes are rapidly decaying with the rank of the partial, so that, to a certain extent, one can say that the radiation efficiency compensates the reduction of magnitude due to the vibration.

Finally, we should bear in mind that, due to the spatial coincidences, the radiated acoustic energy is concentrated in narrow directivity lobes in the supersonic case.

13.4.3.4 Generalization to Multimode Systems

In Sect. 13.4.3.1, the radiated power was calculated for a single mode. We consider now a general motion of the plate expanded onto its in vacuo eigenmodes basis, and written in the form:

$$W(x,y,\omega) = \sum_{m=1}^{\infty}\sum_{n=1}^{\infty} A_{mn}(\omega)\phi_{mn}(x,y) \;=\; {}^t\boldsymbol{A}(\omega)\boldsymbol{\phi}(x,y). \tag{13.119}$$

In what follows, it is assumed that the far field conditions are valid, so that the spatial Fourier transform can be used. Advantage will be taken, in particular, of Parseval's theorem which states that the mean radiated power $\langle \mathscr{P}_a(\omega) \rangle$ can be calculated in the wavenumber space as follows [40]:

$$\langle \mathscr{P}_a(\omega) \rangle = \frac{1}{8\pi^2} \int_{S_r} \mathscr{R}e \left\{ \tilde{P}(k_x, k_y, \omega) \dot{\tilde{W}}^\star(k_x, k_y, \omega) \right\} dk_x dk_y, \tag{13.120}$$

where the "$\star$" symbol designates the conjugate of a variable. For simplicity, the calculation of the power in (13.120) is restricted here to a summation over the quarter circle S_r, which corresponds to the surface modes. In practice, this means that the power radiated by the edge and corner modes are neglected. Using Euler equation, $\langle \mathscr{P}_a(\omega) \rangle$ can be expressed in terms of pressure:

$$\langle \mathscr{P}_a(\omega) \rangle = \frac{1}{8\omega\rho\pi^2} \int_{S_r} |\tilde{P}(k_x, k_y, \omega)|^2 \, k_z \, dk_x dk_y, \tag{13.121}$$

where $k_z = \sqrt{k^2 - k_x^2 - k_y^2}$.

Radiation Resistances Matrix

The radiated power can also be expressed in terms of plate velocity:

$$\langle \mathscr{P}_a(\omega) \rangle = \frac{\omega\rho}{8\pi^2} \int_{S_r} \frac{|\dot{\tilde{W}}(k_x, k_y, \omega)|^2}{k_z} \, dk_x dk_y. \tag{13.122}$$

Using the modal expansion (13.119), the square modulus of the velocity is written equivalently:

$$|\dot{\tilde{W}}(k_x, k_y, \omega)|^2 = |{}^t\dot{\boldsymbol{A}}(\omega) \tilde{\boldsymbol{\phi}}(k_x, k_y)|^2 = \dot{\boldsymbol{A}}^H(\omega) \, \tilde{\boldsymbol{\phi}}^\star(k_x, k_y) \, {}^t\widetilde{\boldsymbol{\phi}}(k_x, k_y) \, \dot{\boldsymbol{A}}(\omega), \tag{13.123}$$

where the exponent "H" accounts for the Hermitian (conjugate transpose) operator. Finally, we get the (supersonic) radiated acoustic power:

$$\langle \mathscr{P}_a(\omega) \rangle = \dot{\boldsymbol{A}}^H(\omega) \mathbb{R}_a(\omega) \dot{\boldsymbol{A}}(\omega), \tag{13.124}$$

where $\mathbb{R}_a(\omega)$ is the *radiation resistance matrix* defined as:

$$\mathbb{R}_a(\omega) = \frac{\omega\rho}{8\pi^2} \int_{S_r} \frac{\tilde{\boldsymbol{\phi}}^\star(k_x, k_y) \, {}^t\widetilde{\boldsymbol{\phi}}(k_x, k_y)}{\sqrt{k^2 - k_x^2 - k_y^2}} dk_x dk_y. \tag{13.125}$$

Notice that this expression is similar to the one obtained in Sect. 13.2.3 for the elementary case of a beam coupled to a semi-infinite tube.

Each term $(R_a)_{ij} = (R_a)_{mn,m'n'}$ of the matrix $\mathbb{R}_a$ quantifies the *mutual radiation resistance* resulting from the interference between the sound fields created by the modes (m, n) and (m', n'). For (m, n)=(m', n'), the *eigen radiation resistance* are obtained, which are identical to those obtained for isolated modes, and which form the diagonal of the matrix $\mathbb{R}_a$.

For a simply supported rectangular plate, it can be shown that [21]:

$$(R_a)_{mn,m'n'} = \frac{mm'nn'\omega\rho\pi^2}{8L_x^2L_y^2} \times \int_{S_r} \frac{f_{mm'}(k_xL_x)\, f_{nn'}(k_yL_y)dk_xdk_y}{[k_x^2-(m\pi/L_x)^2)][k_x^2-(m'\pi/L_x)^2][k_y^2-(n\pi/L_y)^2)][k_y^2-(n'\pi/L_y)^2]}, \tag{13.126}$$

where the functions $f_{mm'}(k_xL_x)$ are equal to:

$$f_{mm'}(k_xL_x) = \begin{cases} 2(1-\cos k_xL_x) & \text{for } m \text{ even}, \quad m' \text{ even}; \\ 2(1+\cos k_xL_x) & \text{for } m \text{ odd}, \quad m' \text{ odd}; \\ 2\sin k_xL_x & \text{for } m \text{ odd}, \quad m' \text{ even}; \\ 2\sin k_xL_x & \text{for } m \text{ even}, \quad m' \text{ odd}. \end{cases} \tag{13.127}$$

Recall that, so far, the action of the sound field on the plate is ignored. This assumption is justified for a light fluid. However, as seen for the infinite plate, the dispersion equation of the plate is otherwise modified (as for a thin and flexible plate, for example). This, in turn, modifies the real and imaginary part of the wavenumbers, due to both the inertia of the fluid and radiation losses. In Chap. 14, the action of the sound field on timpani membranes will be presented, showing substantial modifications of the eigenmodes, compared to the in vacuo case.

13.4.3.5 Radiation Modes of a Plane Plate

The radiation matrix $\mathbb{R}_a(\omega)$ defined in Eq. (13.125) contains the eigenresistances of each structural mode on its diagonal and, on both sides, the mutual radiation resistances. As a consequence, it is not possible to control the power radiated by each structural mode independently from the others, because of the intermodal coupling. The problem of the vibratory and acoustic control of musical instruments is a rapidly evolving field [18], and thus it is worth to take time for addressing this question. In addition, this problem yields important theoretical results.

The goal is to determine whether velocity distributions exist on the plate so that the power radiated by each of them is independent from the others. These velocity distributions are the *radiation modes* of the plate [12]. Since $\mathbb{R}_a(\omega)$ is symmetrical,

definite and positive, it can be decomposed as follows:

$$\mathbb{R}_a = {}^t\mathbb{P}\mathbb{L}\mathbb{P}, \tag{13.128}$$

where $\mathbb{L}$ is a diagonal matrix whose elements on its diagonal are the eigenvalues of $\mathbb{R}_a$. The matrix $\mathbb{P}$ is the transfer matrix (the matrix of the eigenvectors). Following (13.124), the radiated acoustic power can be rewritten as follows:

$$\langle P_a(\omega)\rangle = \mathbf{b}^H\mathbb{L}\mathbf{b} \quad \text{where} \quad \mathbf{b} = \mathbb{P}\dot{\mathbf{A}}. \tag{13.129}$$

One can check that Eq. (13.129) is written explicitly:

$$\langle P_a\rangle = \sum_n L_n|b_n|^2, \tag{13.130}$$

which shows that the radiating modes b_n are independent from each other. L_n is the radiation efficiency associated to the n-th radiated mode.

One difficulty in the use of the radiation modes is due to the dependence of $\mathbb{R}_a$ with frequency. This means that the calculation of these variables has to be made again for each frequency of interest. However, several authors have shown that, for $ka \ll 1$ where a is a characteristic dimension of the plate, the radiation modes are reasonably well independent of frequency. Figure 13.28 shows the six first radiation modes of a baffled plane plate, calculated by Elliott and Johnson [12]. The first mode is identical to the mode of a plane piston. It corresponds to the monopole component of the plate whose flow rate is given by the product of the surface by the mean velocity. The detailed calculation of the eigenvalues and eigenvectors show that this lowest mode contains the main part of the radiated power. The radiation efficiency of the higher-order radiation modes is much lower.

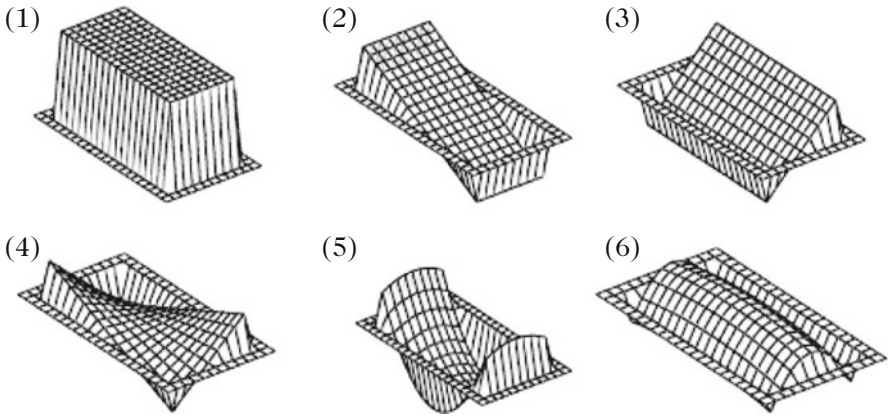

Fig. 13.28 First radiation modes for a rectangular baffled plate. $kL \approx 0.1$. After [12]

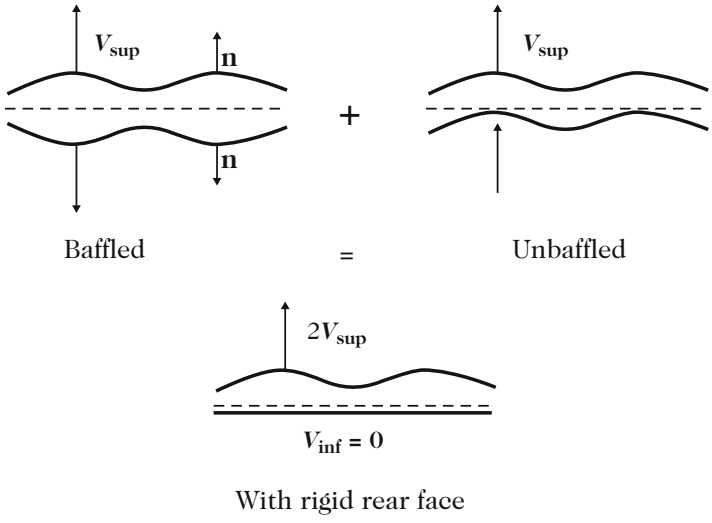

Fig. 13.29 Decomposition of a volume with plane walls into several planar sources. After [24]

13.4.4 Radiation of Unbaffled Plates and Structural Volumes

To a first approximation, stringed musical instruments can be viewed as structural volumes with one (or more) vibrating sides. For simplicity, it is assumed here that the vibrating parts of the volume are plane surfaces. Figure 13.29 shows a particular case where only the upper surface of the volume vibrates, all other surfaces remaining at rest. This simplified model is close to the case of a guitar where the vibrations of neck, sides, and back plate would be neglected compared to the vibrations of the soundboard.

The radiation of a volume composed of planar walls can be decomposed into two parts: a *baffled* plate part and an *unbaffled* plate part. As seen in Chap. 12, a baffled source has a condition of zero velocity on the rigid baffle containing the source, and thus the system is equivalent to two moving plates with symmetrically opposite velocities on both sides of the baffle. In contrast, an oscillating unbaffled source can be viewed as the association of two plates moving in phase. As a consequence, as shown in Fig. 13.29, the pressure radiated by a volume with one moving plane wall is the sum of two contributions: one pressure p_b generated by the baffled component, and a pressure p_u radiated by the unbaffled component. This property incited us to study first the radiation of unbaffled plates, for which the direct use of the Rayleigh integral is not valid anymore.

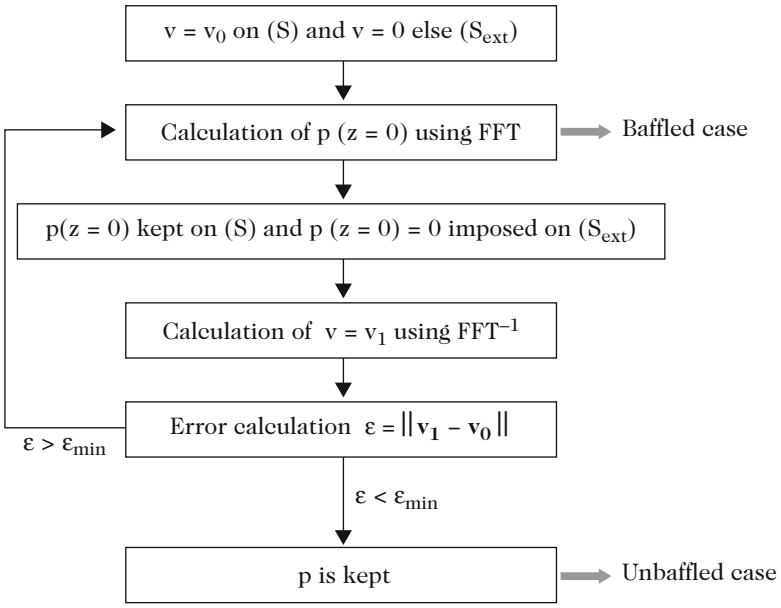

Fig. 13.30 Iterative algorithm for the calculation of the pressure radiated by an unbaffled plane plate. After [39]

13.4.4.1 Radiation of an Unbaffled Source: Iterative Algorithm

The method presented below was developed in the 1980s by Williams and Maynard [39]. This method takes advantage of the spatial Fourier transform presented in Sect. 13.4, which means that it is restricted to the prediction of far field radiation. In practice, the Fourier transforms are calculated numerically on a discrete mesh of the structure and, in turn, on a discrete set of wavenumbers. Using rapid and appropriate tools, such as the Fast Fourier Transform (FFT), a good estimate of the pressure can be rapidly obtained, even in the case of complex vibration patterns. The successive steps of the iterative algorithm used for the computation of the sound field are shown schematically in Fig. 13.30.

(1) Let us denote v_0 the velocity imposed on the baffled plate. The remaining part of the infinite plane (baffle) is supposed to be perfectly rigid ($v = 0$). In a first step, the radiated pressure field p_0 in the space is then calculated by means of the Rayleigh integral (using, for example, the FFT).
(2) In a second step, the pressure field p_0 is retained, except on the baffle, where the condition $p = 0$ is imposed. Through inverse Fourier transform, the velocity field v_1 is calculated corresponding to this modified pressure distribution.
(3) The velocity field v_1 is compared to the initial (given) velocity profile v_0. If the relative error ε between these two velocity fields is larger than an arbitrarily

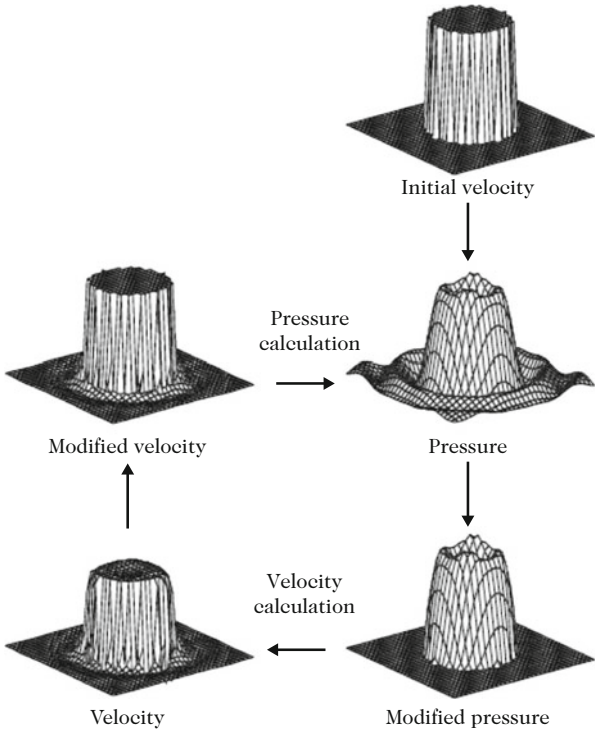

Fig. 13.31 Iterative calculation of the pressure radiated by an unbaffled plane piston of radius a, for $ka = 4$. After Le Pichon [24]

imposed limit $\varepsilon_{\min}$, then another iteration occurs. Otherwise, it is considered that the result corresponds to the imposed boundary conditions, and the calculation stops.

In practice, it is observed that the algorithm converges rapidly for $ka > 1$, where a is a characteristic dimension of the plate. Figure 13.31 shows, for example, the results obtained for a unbaffled plane piston for $ka = 4$.

13.4.4.2 Application to the Guitar

The previous method was successfully applied to the guitar by Le Pichon [25]. First, the velocity profile of both the soundboard and back plate of the instrument were measured. For each of these two vibrating surfaces, the radiated sound field was calculated by summing two contributions: the first (for the baffled component) with the Rayleigh integral, and the second (unbaffled component) by means of the iterative algorithm presented above.

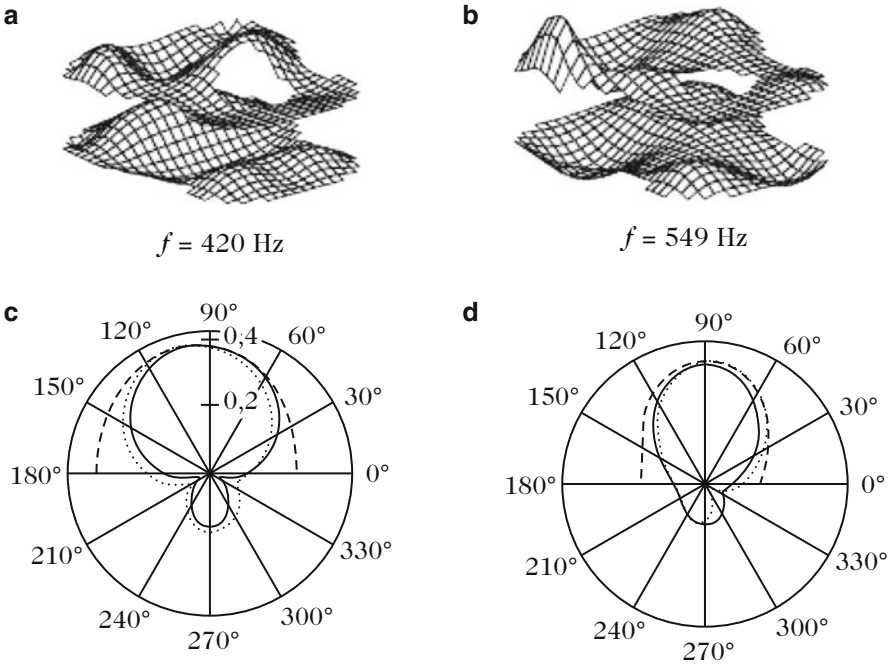

Fig. 13.32 Comparison between measurements and prediction of guitar directivity patterns at two frequencies: 420 and 549 Hz. The measured velocity profiles of soundboard and back plates are shown in (**a**) and (**b**). The corresponding directivity patterns are shown in (**c**) and (**d**). On these two diagrams, the directivity predicted by the Rayleigh integral applied to the soundboard only is represented with a *dashed line*. The directivity patterns predicted by the volume model, taking both plates into account are drawn with *solid lines*. Finally, the directivity patterns measured in an anechoic chamber are in *dotted lines*. After [25]

Figure 13.32 shows the calculated directivity patterns, and the comparison with measurements performed in an anechoic chamber. It can be seen, among other things, that the baffled plate model (Rayleigh integral) yields erroneous predictions, especially on the back of the instrument. In contrast, the measured directivity is well predicted by the *volume* model. In accordance with the properties of the iterative algorithm, the results obtained with this method are deteriorated in the low frequency range (for $ka < 1$). For a guitar, the typical frequency limit is around 60 Hz. Also recall that the method is not applicable in the near field.

13.5 Radiation of an Axisymmetrical Nonplanar Source

For a number of instruments, the radiating body is not a plate but a shell which is, by definition, a nonplanar source. Such a shape is justified by several reasons. It was shown, for example, in Chap. 8 that the curvature of gongs and cymbals is

the prime origin of the quadratic nonlinearities observed in the sounds of these instruments, in case of large amplitude motion. In bowed strings instruments, the curvature of the soundboard allows the conversion of the vertical static loading due to the tension of the strings into a "membrane-like" prestress in the soundboard. As a consequence, the soundboard is more rigid, which contributes to increase the radiation efficiency, and, in addition, this geometry yields a better contact between the bridge and the strings. Finally, in wind instruments, several authors have shown that, in some situations, a coupling exists between the sound field and the structure [13, 14, 22, 27, 29]. In this case, the tubular geometry of the tubes also is described by a shell model.[10]

In this section, the influence of the curvature on the radiation properties of a source are examined, and the differences with the case of planar sources are highlighted. First, some simple rules are derived from the dispersion curves, which show the effect of the curvature on the radiation efficiency. In a second step, it is shown to what extent the curvature modifies the radiated pressure, compared to the case of a plate. A simplified model is presented, in case of shallow shells, which can be used for many instruments. Based on a modal approach, the notion of *Spatial impulse response* is presented. The general concepts are illustrated on the particular case of the spherical shallow shell, which is typical example of practical use in many percussive instruments, and which can also account for the radiation of some loudspeakers and stringed instruments. The effect of the curvature on both the directivity of the source and cutoff frequency are particularly emphasized.

13.5.1 Dispersion Curves for Shells and Critical Frequency

Figure 13.33 shows an example of spherical shell with radius of curvature R, and the associated dispersion curve. For thin shallow shells, the dispersion relation is given by [34]:

$$\rho_s h\omega^2 = Dk^4 + \frac{Eh}{R^2}, \tag{13.131}$$

where ρ_s is the density of the shell, and h its thickness. It can be seen in Fig. 13.33 that the dispersion curve is shifted up, compared to the case of plates [Eq. (13.49)]. The shift of the curve increases when R decreases. The curvature tends to make the structure stiffer. As a consequence, the critical frequency decreases, which is shown by the position of the intersection point between both dispersion curves. In addition, due to the presence of a constant term in (13.131), another intersection point appears near the origin of the axes. This indicates that the second effect of the

[10]The issue of the material choice for wind instruments is a very intricate and controversy matter. Two different materials handled by the same tool do not produce the same geometry, and the nature of the material intervenes also by its porosity, the state of its surface, its heat capacity, etc.

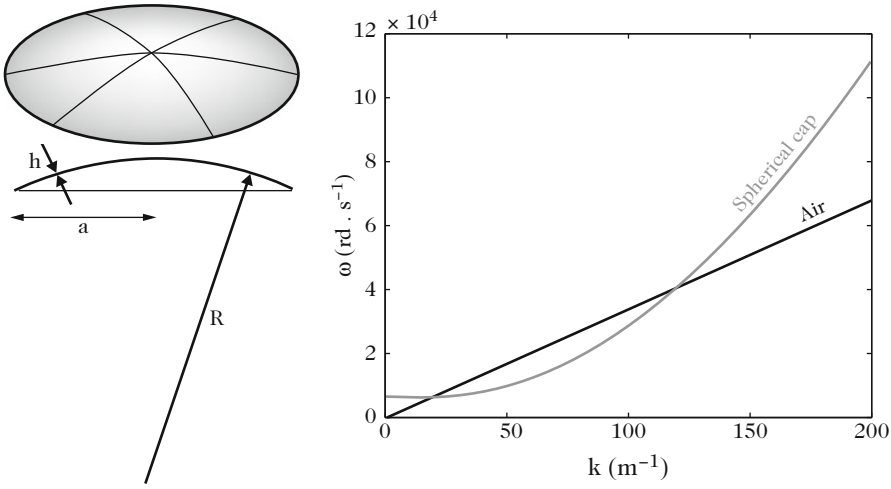

Fig. 13.33 Spherical cap and its associated dispersion curve. The *straight line* in the (ω, k)-diagram accounts for the air dispersion. The numerical values selected for this example are: $E = 2 \times 10^{11}\,\mathrm{N\,m^{-2}}$, $\rho_s = 7.8\,\mathrm{kg\,m^{-3}}$, $R = 0.8\,\mathrm{m}$, $h = 2\,\mathrm{mm}$, and $\nu = 0.3$

curvature is to enhance the radiation efficiency in the low-frequency range. For a small radius of curvature, a situation may occur where the dispersion curve of the shell is completely above the dispersion curve of the air: in this case, there is no critical frequency anymore and all structural modes are radiating.

Similar results are obtained for thin cylindrical shallow shells, such as the one shown in Fig. 13.34, where a is the radius of curvature. Denoting ω_p the corresponding plate modes (obtained in the limiting case of an infinite radius of curvature), it can be shown that the cylindrical shell modes fulfill the relation [34]:

$$\omega_s^2 = \omega_p^2 + \frac{E}{a^2 \rho_s (1 - \nu^2)}. \tag{13.132}$$

As a consequence, similar conclusions as for the spherical shell can be drawn here. In particular, all modes will be radiating when the dispersion curve of the cylindrical shell is located above the air dispersion curve, which can occur for a small radius of curvature.

13.5.2 Radiated Pressure

Let us now turn to the exact calculation of the pressure radiated by shells. For simplicity, we limit ourselves here to axisymmetrical shells. Figure 13.35 shows that, by contrast to the case of plane plates, the structural velocity might not be normal to the structure. In the general case, we have to take both the normal v_n and

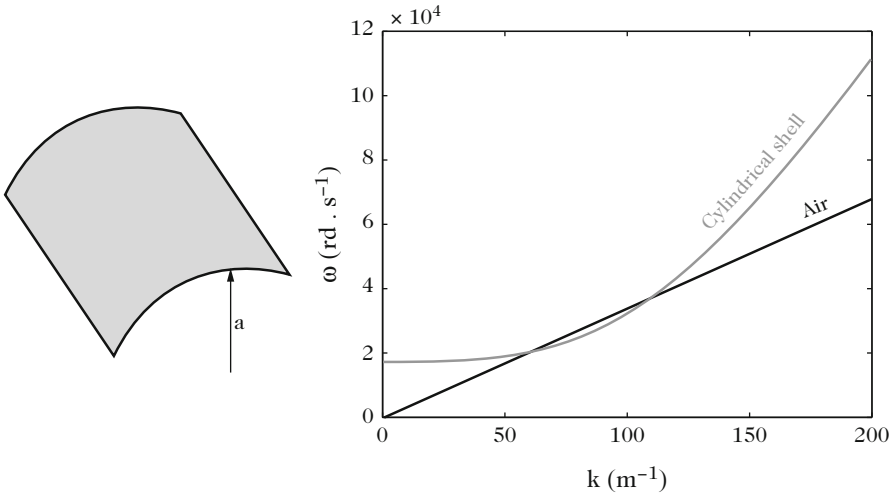

Fig. 13.34 Cylindrical shell and its associated dispersion curve. $E = 2 \times 10^{11}\,\mathrm{N\,m^{-2}}$, $\rho_s = 7.8\,\mathrm{kg\,m^{-3}}$, $a = 0.3\,\mathrm{m}$, $h = 2\,\mathrm{mm}$, and $\nu = 0.3$

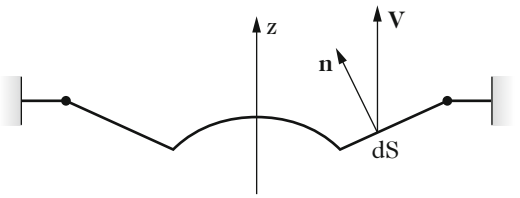

Fig. 13.35 Example of an axisymmetrical structure of axis z

the tangential v_t velocity into account. The complete calculation of the Kirchhoff–Helmholtz integral in this case was done by Hu and Wu [20]. These authors show that the pressure is then given by the sum of four terms:

$$p(\mathbf{r},t) = \mathscr{M}_n(\mathbf{r},t) + \mathscr{M}_t(\mathbf{r},t) + \mathscr{D}_n(\mathbf{r},t) + \mathscr{D}_t(\mathbf{r},t), \tag{13.133}$$

where $\mathscr{M}_n$ and $\mathscr{D}_n$ are the monopole and dipole contributions of the normal velocity, respectively, whereas $\mathscr{M}_t$ and $\mathscr{D}_t$ are the monopole and dipole contributions of the tangential velocity. For a shallow shell inserted in an infinite baffle, this sum reduces to the first term, which is of the Rayleigh type, though with a nonplanar integration surface. This term is written in the time-domain:

$$p(\mathbf{r},t) = -\rho \int_0^t \int_S g(\mathbf{r},\mathbf{r}',t,\tau)\frac{\partial v_n(\mathbf{r}',\tau)}{\partial \tau} dS_{\mathbf{r}'} d\tau, \tag{13.134}$$

where $g(\mathbf{r},\mathbf{r}',t,\tau)$ is the space-time Green's function. For a known (imposed) normal velocity v_n, the problem reduces to the appropriate determination of the Green's function g. This function is here different from the one defined in Chap. 12

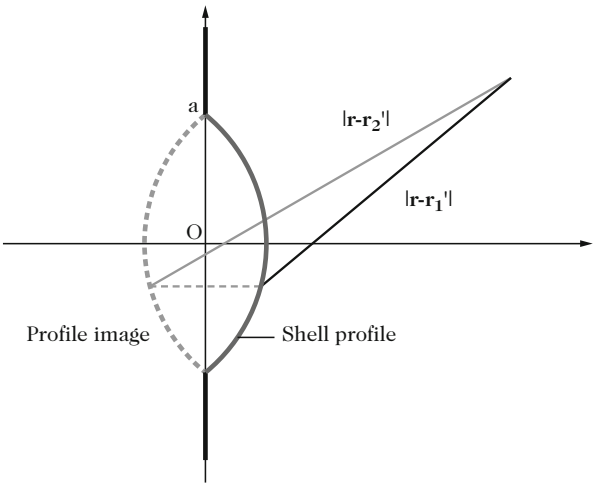

Fig. 13.36 Construction of the Green's function for a spherical cap

for the plane piston, because of the curvature of the source. Figure 13.36 shows a example of graphical construction of a Green's function for a spherical cap, using the method of images.

For a shell inserted in an infinite rigid baffle, the condition of zero velocity on the baffle imposes

$$\begin{aligned} g(\mathbf{r},\mathbf{r}',t,\tau) &= g_1(\mathbf{r},\mathbf{r}',t,\tau) + g_2(\mathbf{r},\mathbf{r}',t,\tau) \\ &= \frac{\delta(t-\tau-|\mathbf{r}-\mathbf{r}'_1|/c)}{4\pi|\mathbf{r}-\mathbf{r}'_1|} + \frac{\delta(t-\tau-|\mathbf{r}-\mathbf{r}'_2|/c)}{4\pi|\mathbf{r}-\mathbf{r}'_2|}, \end{aligned} \quad (13.135)$$

where the first term g_1 is the contribution of the direct sound, while the second term g_2 is the contribution of the reflection from the source. Once the Green's function is known, the calculation continues by using a modal approach. The transverse displacement w of the shell is expanded onto its in vacuo eigenmodes basis. We write

$$w(\mathbf{r},t) = \sum_{p=0}^{\infty} \Phi_p(\mathbf{r}) q_p(t), \quad (13.136)$$

where $q_p(t)$ are the generalized displacements. The modal decomposition of the pressure is derived

$$p(\mathbf{r},t) = -\rho \sum_{p=0}^{\infty} \int_0^t \int_S g(\mathbf{r},\mathbf{r}',t,\tau)\Phi_p(\mathbf{r}')\ddot{q}(\tau)\, \mathbf{e_z}.\mathbf{dS}_{\mathbf{r}'}\, d\tau, \quad (13.137)$$

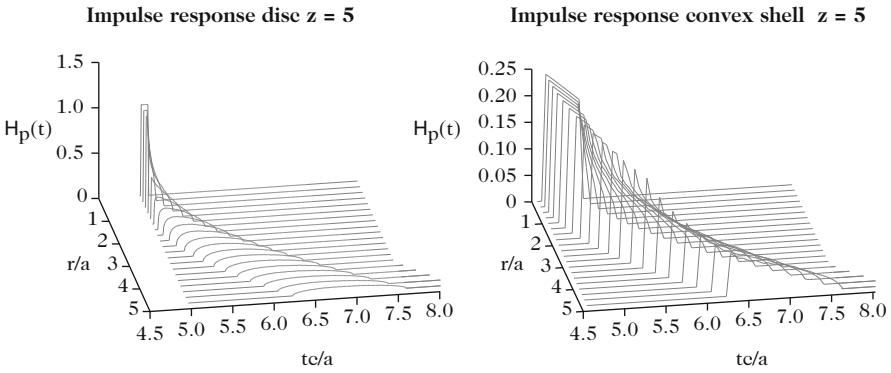

Fig. 13.37 Spatial impulse response for the planar piston (*left*) and a convex spherical cap (*right*)

in the particular case of a velocity profile of the shell oriented in the direction $\mathbf{e_z}$ of the shell axis (see Fig. 13.35). One main interest of the expression (13.137) is that it remains valid even for nonlinear vibrations, which is usually the case for gongs and cymbals, as shown in Chap. 8 [30]. This property results from the fact that no particular condition is given above on the displacements $q(t)$. Another interesting property results from the grouping of the terms g and Φ under the integral, which yields, after integration, to the following transformation:

$$p(\mathbf{r}, t) = -\rho \sum_{p=0}^{\infty} \int_0^t \mathscr{H}_p(\mathbf{r}, \tau) \ddot{q}(\tau) d\tau. \tag{13.138}$$

This method was originally developed by Stepanishen [35]. The function $\mathscr{H}_p$ was called *Spatial Impulse Response, or SIR* for the mode p by the author. This function contains together the information on the modal shape for the mode p and on the observation point $\mathbf{r}$, for a given shell profile.

Figure 13.37 shows a comparison between two spatial impulse responses, for the plane piston and a convex spherical cap. These plots show the spreading of the response over time when the observer moves in a vertical plane at a fixed distance from the source plane (baffle). One can see, in particular, that this spreading is more pronounced for the spherical cap than for the plane piston, which, as we will show in the next paragraph, implies that the cutoff frequency of the pressure spectrum is lower for the cap, compared to a piston of the same size.

13.5.3 Influence of the Source Shape

The shape of a source influences both the directivity and bandwidth of its radiated sound pressure. These effects can easily be shown in the frequency domain, through calculation of the Fourier transform of the spatial impulse response. Figure 13.38

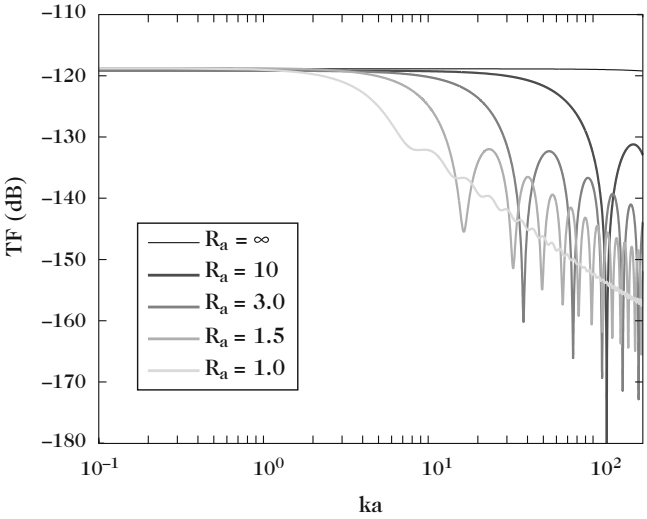

Fig. 13.38 Far field pressure response curves on the axis for different spherical caps with different radii of curvature. $R_a = R/a$ is the dimensionless ratio between the radius of curvature and the radius of the circle obtained through projection of the cap on a plane. The cutoff frequency decreases as the radius of curvature decreases. The curvature has thus a *lowpass filter* effect on the radiated pressure. After [30]

shows, for example, the frequency response of the far field pressure on the axis (at a distance equal to 100 times the radius of the source) for a spherical cap with different radii of curvature. One can see that the cutoff frequency of the response decreases as the radius of curvature increases.[11] Another feature to notice is that a kind of *comb filter* effect appears in the attenuated band.[12]

In contrast, Fig. 13.39 shows that the directivity in the far field is less pronounced for convex spherical caps, at a given frequency, as the radius of curvature decreases. The convexity of the source thus spreads the acoustic pressure more uniformly in space, the price to pay being a reduction of the pressure magnitude with frequency. These properties have direct consequences from the point of view of sound distribution and sound reproduction in a room: a source with a curvature seems to be more appropriate if the purpose to insonify a zone for a large audience.

[11] By analogy with the electric filters, this cutoff frequency can be defined as the value for which the pressure is reduced by a factor of −3 dB compared to its low-frequency asymptotic value (see Fig. 13.38).

[12] Similar results were obtained by Suzuki and Tichy [37], using the theory of spherical harmonics for expanding the pressure (see Chap. 12). These authors report that, due the diffraction effects, an attenuation of the order of −5 dB between $ka = 0.4$ and $ka = 4$ is obtained for the convex caps, whereas an amplification of 4 dB is obtained for the concave case.

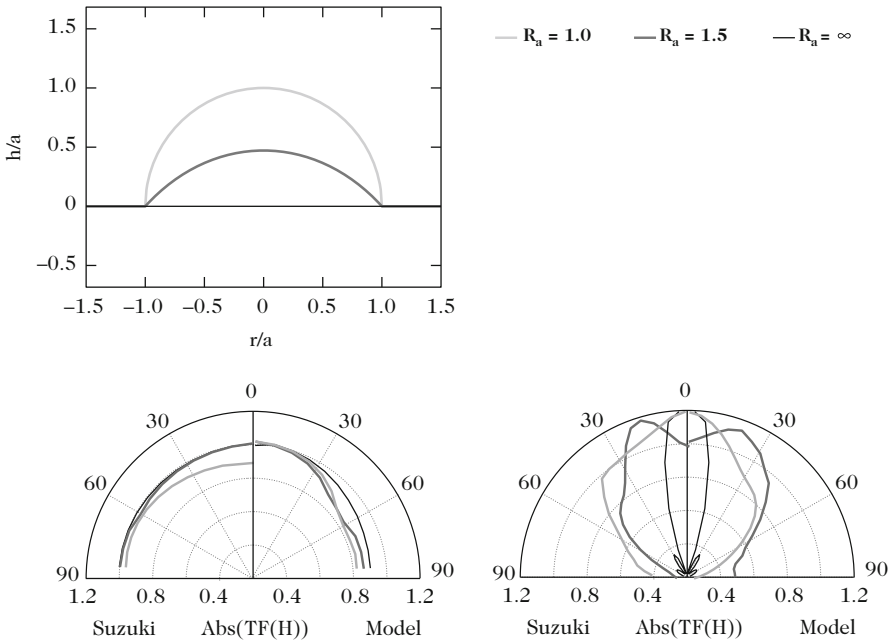

Fig. 13.39 Far field directivity patterns of some convex spherical caps at two frequencies corresponding to $ka = 1$ and $ka = 10$. The profile of the caps are drawn in *black* and *gray* colors in figure (**a**) (*top*). The model presented in this chapter is compared to the work by Suzuki [37]. (**b**) and (**c**) (*bottom*) are symmetrical about the axis $\theta = 0°$. The Suzuki model is on the *left* side of the axis and the present model on the *right*

13.6 Application to Stringed Instruments

In this section, the purpose is to show how some fundamental results of vibroacoustics can be applied to stringed instruments. The presentation starts by specifying to what extent the concepts of critical frequency and modal density, together with the mechanical impedance of the soundboard, are of help in selecting the appropriate materials for enhancing the acoustical efficiency of the instrument. It is followed by the experimental analysis of a piano soundboard which illustrates the analytical results on efficiency and radiation resistance. Finally, the necessary compromise that is to be found between loudness and tone duration for free oscillations systems, such as the piano or the guitar, is discussed.

13.6.1 Selection of Materials and Merit Index

The addressed question here is how to select the appropriate material for building stringed instruments. The demonstration below is inspired from the work by Barlow [4]. First, we focus on the acoustical efficiency of stringed instruments. The underlying idea is to show under which conditions the mechanical power transmitted by the strings to the bridge can be usefully converted into acoustical power. This imposes to lower the critical frequency while keeping the real part of the admittance at the bridge as high as possible. In Sect. 13.3.3, the critical frequency was calculated in the case of an isotropic material [see Eq. (13.51)], and the usually admitted approximate formula for orthotropic materials also was indicated

$$f_c \approx \frac{c^2}{\pi h}\sqrt{\frac{3\rho_p(1-\nu^2)}{[E_1E_2]^{1/2}}}. \tag{13.139}$$

In Sect. 13.3.7.1, the driving-point impedance was calculated for an infinite isotropic plate, and the approximate expression for an orthotropic plate also was given. In terms of admittance (or mobility), this quantity is written:

$$Y_p \approx \frac{1}{4h^2}\sqrt{\frac{3(1-\nu^2)}{\rho_p[E_1E_2]^{1/2}}}. \tag{13.140}$$

Recall that Eq. (13.140) also corresponds to the mean (and asymptotic) value of the admittance for a finite plate [33] and this is the reason why it is well adapted to our problem. Assuming further that the Poisson's coefficients have a minor effect on the admittance, one can see that both quantities in Eqs. (13.139) and (13.140) basically depend on the thickness h and density ρ, and on the Young's moduli of the plate.

First of all, it is reasonable to consider that the thickness h of the soundboard is selected in such a manner that the spectral domains of strings and soundboard, respectively, coincide. Otherwise, the instrument would not have the possibility to enhance the vibrations of the strings. Once the thickness has been fixed, then only the two parameters of the soundboard material remain to be optimized. By eliminating h between both quantities Y_p and f_c, a *merit index* is obtained

$$\mathrm{M_e} = \frac{Y_p}{f_c^2} = \frac{\pi^2}{4c^2\sqrt{3(1-\nu^2)}}\frac{[E_1E_2]^{1/4}}{{\rho_p}^{3/2}}. \tag{13.141}$$

Equation (13.141) shows that, in order to maximize the acoustical power radiated by the plate, the quantity $[E_1E_2]^{1/2}/\rho_p^3$ needs to be maximized also. For an isotropic plate, this quantity reduces to E/ρ_p^3. One convenient strategy to make the most of this result is to use the well-known Ashby diagram [3] shown in Fig. 13.40.

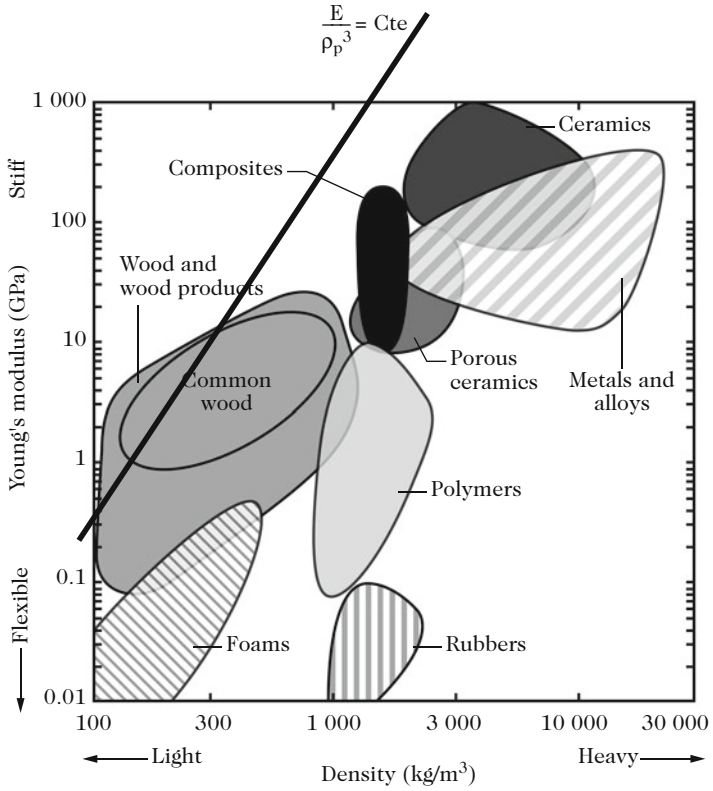

Fig. 13.40 Ashby diagram. After [3]

In this diagram, the density is represented on the horizontal axis, while the Young's modulus is shown on the vertical axis, in logarithmic coordinates, for a large class of materials. For the purpose of the demonstration, a zone called *mean wood* is added on the diagram, where the elastic moduli are the mean values $E_{moy} = [E_1 E_2]^{1/2}$ of the usual wood species used in lutherie. Imagine now a line of constant slope $E/\rho_p{}^3$ translating on this diagram. It can be seen that this quantity is maximized in the region of the diagram corresponding to low density and high moduli: as a conclusion the best candidate to build an instrument ... is the wood !

Examining the Ashby diagram more closely shows that the "winner," for this merit index, is the balsa wood. However, this result needs to be tempered, since other criteria have to be considered in instrument making. The yield strength, in particular, imposes maximal values for the stresses in the structure in terms of traction, compression and shear. Other Ashby materials are available where such a criterion is taken into account. In practice, breakable wood species, such as balsa wood, are not appropriate for soundboard, in view of the usual static loading they have to withstand. For more information on the properties of wood in string instruments, one can refer to [6].

Function of the Modal Density

In the previous paragraph, the selection of materials for stringed instruments was based on the critical frequency. Another alternative for the reasoning is to use the concept of modal density, which yields another appropriate criterion in the case of finite plates. In Chap. 3, it was shown that the radiated acoustical power is proportional to the real part of the admittance and, in turn, to the modal density of the plate. For an orthotropic rectangular plate of surface S, the following approximate formula was obtained

$$D(f) \approx \frac{S}{h}\sqrt{\frac{3\rho_p(1-\nu^2)}{[E_1E_2]^{1/2}}}, \tag{13.142}$$

which is proportional to the critical frequency. Bringing together Eqs. (13.140) and (13.142), we get

$$D(f) = 4Y_pSh\rho_p = 4Y_pM_{\text{tot}}, \tag{13.143}$$

where M_{tot} is the total mass of the plate. For a finite plate, Y_p should be here considered as the (real) asymptotic value of the admittance in the high frequency range or, equivalently, as the mean value of the admittance over the frequency range of interest radiated by the plate [33].

In Chap. 6, it was shown that the power transmitted from the strings to the soundboard to the real part of the admittance, for a given transverse force. Equation (13.143) shows, in addition, that this admittance's real part is proportional to the modal density and inversely proportional to the total mass of the plate.

13.6.2 Example of the Piano Soundboard

The concepts of radiated power, radiation resistance, and acoustical efficiency are now illustrated by using the piano soundboard as an example. We take advantage here of the experimental results obtained by Suzuki [36].

Figure 13.41 shows the results of measurements conducted with wideband excitation. The mean radiated power was calculated by means of the flow of the acoustic intensity vector through a surface S of the soundboard $I = 1/2\mathscr{R}e\{PV^\star\}$. In these experiments, the pressure is measured in the near field, close to the soundboard, and the acoustic velocity V is derived from the measurements of the soundboard velocity. The excitation force is normalized to 1 N. Between 50 and 500 Hz, the radiated power is weak, except at some frequencies corresponding to the eigenmodes of the soundboard. The power increases progressively between 500 and 2000 Hz, with a maximum in the range 1800–2000 Hz. The power remains constant above 2 kHz. It is interesting to compare the power to the radiation efficiency shown

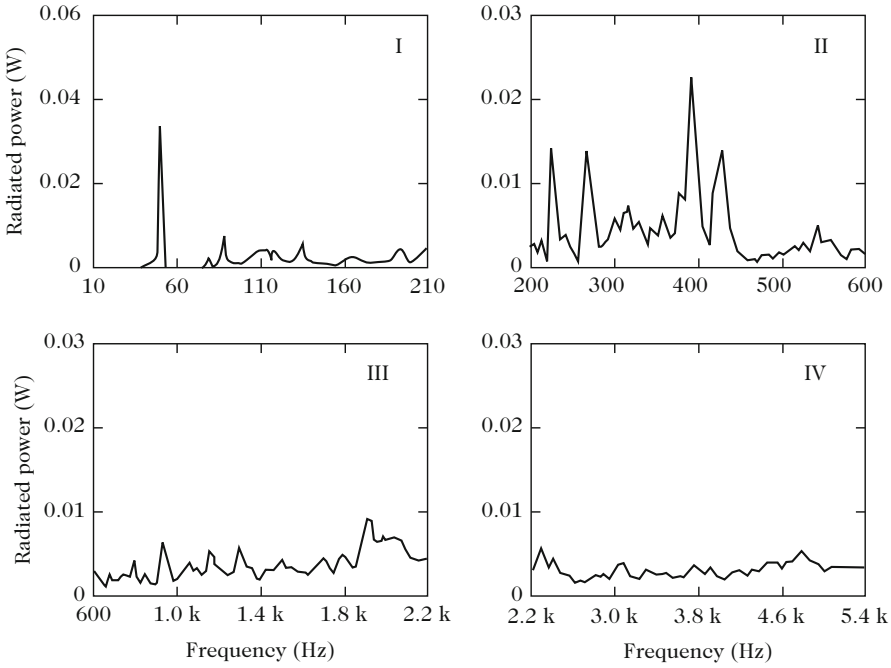

Fig. 13.41 Measurements of the acoustical power radiated by a soundboard, in four different frequency bands. After [36]

in Fig. 13.42. Recall that the efficiency is defined as the ratio between acoustical power and the mechanical power at the input. Some differences exist between both curves, although the general tendency is comparable. The efficiency is almost constant above 1.4 kHz, and decreases slightly above 3.5 kHz. By comparison with the theoretical results, one can reasonably estimate on these figures that the critical zone is approximately situated between 1.2 and 1.6 kHz. In addition, an estimation based on typical values, such as $E = 1.4 \times 10^{10}\,\mathrm{N/m^2}$ for the mean Young's modulus, $\rho_p = 400\,\mathrm{kg/m^3}$ for the density, and a mean thickness equal to 9 mm yields a critical frequency equal to 1.2 kHz, which is coherent. One can assume, in addition, that the internal losses in the wood increase above 3.5 kHz, thus contributing to reduce the efficiency in this range. Another explanation given by the author is based on the experimental conditions, as a result of the distance (a few centimeters) between the measurements points of velocity and pressure, respectively.

The Suzuki paper also shows the input power versus frequency (not shown here). This shows, in particular, that the input power is high around the eigenmodes of the soundboard, especially in the low-frequency range. One can remark that this situation is rather fortunate since, in this range, the rather high level of vibration is compensated by a smaller efficiency, compared to the high frequency range (above

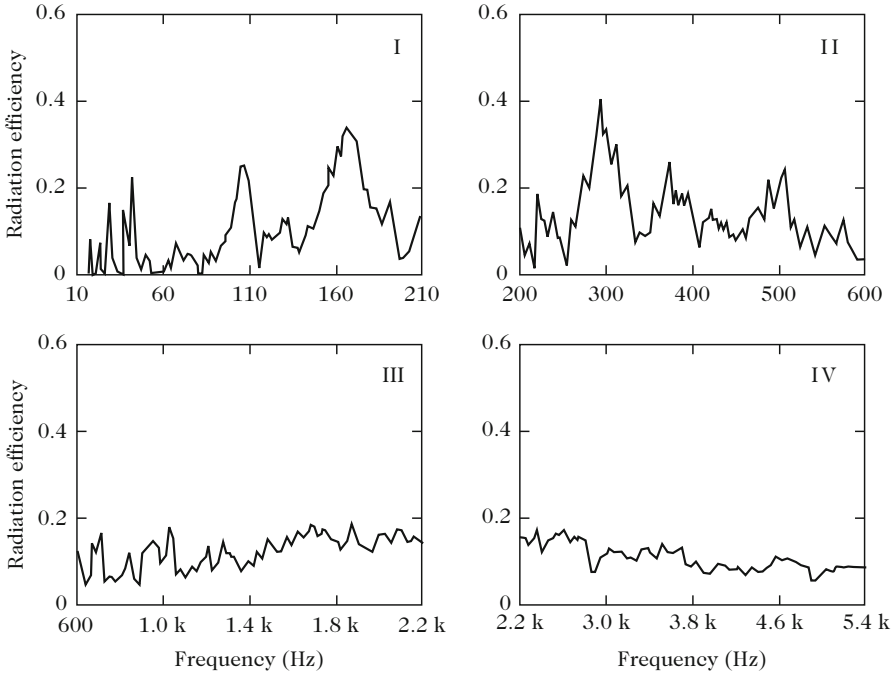

Fig. 13.42 Measurements of the radiation efficiency of a piano soundboard in the same frequency range as in Fig. 13.41. After Suzuki [36]

the critical frequency). As a result, the sound power in the complete range of the piano tends to be rather uniform. At this stage, one must add that one of the main difficulty for piano makers is to obtain a sufficiently high acoustic level for the highest notes of the instrument. The limitations here can be due to three possible phenomena: first, the mechanical energy imparted to the string is usually weak in this range. Second, the coupling between string and bridge is strong thus reducing the tone duration (see the next paragraph below). Third, the zone of effective vibration of the soundboard is restricted to a small area (see the paragraphs dealing with the localization of modes in Chap. 3).

Finally, as seen in Eq. (13.117), the normalized radiation resistance $R_a/\rho c$ is defined as the product of the radiation efficiency by the radiating area. This quantity then yields useful information on the radiation efficiency for a given vibrating part of the instrument. In the cited Suzuki paper, the resistance R_a of the piano is presented for the area corresponding to the medium and high frequency range of the instrument (see Fig. 13.43). In this figure, the increase of R_a between 0.6 and 1.8 kHz is seen more clearly than on the complete instrument. Again, a clear negative slope is seen beyond 3.5 kHz.

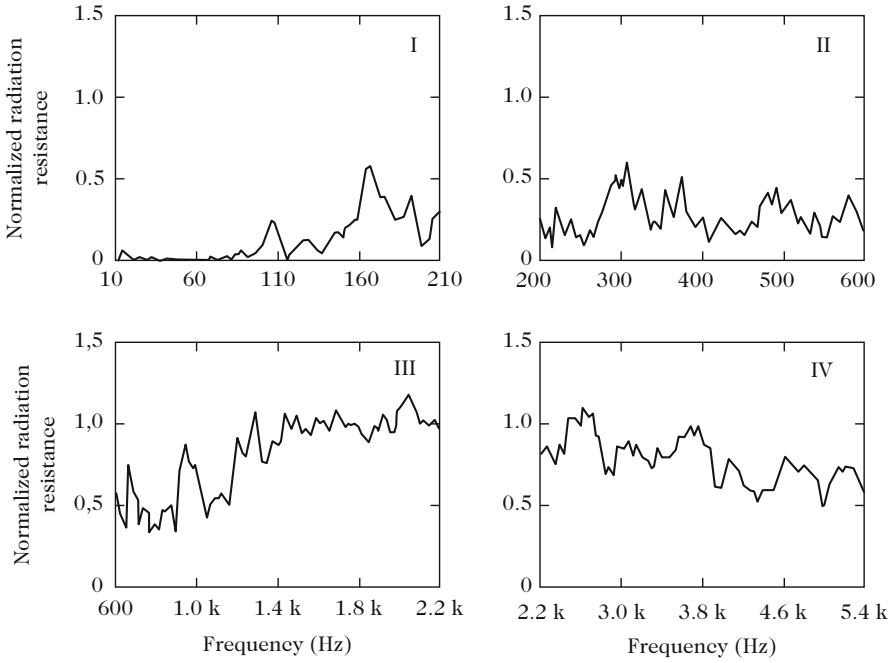

Fig. 13.43 Measurement of the radiation resistance of a piano soundboard, in the restricted area corresponding to the medium and high range of the instrument. After Suzuki [36]

Numerical methods are necessary to calculate the radiation efficiency of a piano accurately (see Chap. 14). However, it has been shown here that qualitative results and relevant trends can be obtained from general considerations based on simple plate models.

13.6.3 Compromise Between Loudness and Tone Duration

In the foregoing, simple criteria were established as guidelines for the selection of materials used for soundboards. These criteria are based on the following quantities: critical frequency, driving-point admittance at the coupling point between soundboard and strings, modal density of the soundboard. The calculations were made with the underlying goal to maximize the radiated power. In the reality, this objective has to be more flexible for free oscillations instruments, such as the piano, the cembalo, or the guitar, for example. This follows from the fact that the tone duration decreases as the radiated power increases, since the radiation damping factor of the soundboard is proportional to the radiated power (see Chap. 6). This situation might, or might not, be desirable, depending on the musical context.

Let us take the example of the piano again. In Chap. 6, it was shown that the damping factor of an isolated string with tension T and length L loaded at one end by an admittance $Y(\omega)$ was given by:

$$\alpha(\omega) = \frac{1}{\tau} = \frac{T}{L}\mathscr{R}e\{Y(\omega)\}. \tag{13.144}$$

In the upper range of a grand piano, the tension T is almost constant and equal to 800 N (see [9]). As a consequence, the damping factor increases if the string's length is reduced, for a given admittance. To compensate this phenomenon, the driving-point mobility should be reduced. This means, for example, in practice that, for a given material, and according to (13.140), the thickness and the rigidity of the soundboard increase near the coupling point. Such an achievement needs a special design, and attention must be paid to the fact that these modifications do not induce other unwanted and unanticipated effects.

In a real instrument, the tone duration is governed by additional phenomena. It was shown in Chap. 6, for example, that both the vertical and horizontal motion of the string are coupled by the motion of the bridge. The input admittance corresponding to the horizontal motion is significantly smaller than the one of the vertical motion (see, for example, [23]). As a consequence, the decay time of the horizontal component of the string is higher that the one of the vertical component, which contributes to increase the tone duration. Other coupling phenomena, such as the coupling of the triplets of strings of a given piano note, influence the duration of a tone significantly.

References

1. Abramowitz, M., Stegun, I.A.: Handbook of Mathematical Functions, with Formulas, Graphs, and Mathematical Tables. Dover, New York (1972)
2. Arcas, K.: Physical model of plate reverberation. In: Proceedings of the 19th International Congress on Acoustics, Madrid (2007)
3. Ashby, M.F.: Materials Selection in Mechanical Design. Butterworth-Heinemann, Oxford (2004)
4. Barlow, C.Y.: Materials selection for musical instruments. In: Proceedings of the Institute of Acoustics, ISMA'97, pp. 69–78 (1997)
5. Boullosa, R.R., Orduna-Bustamante, F., Lôpez, A.P.: Tuning characteristics, radiation efficiency and subjective quality of a set of classical guitars. Appl. Acoust. **59**, 183–197 (1999)
6. Brémaud, I.: Acoustical properties of wood in string instruments soundboards and tuned idiophones: biological and cultural diversity. J. Acoust. Soc. Am. **131**(1), 807–818 (2012)
7. Busch-Vishniac, I.J.: Drive point impedance of an infinite orthotropic plate under tension. J. Acoust. Soc. Am. **71**(1), 368–371 (1982)
8. Chaigne, A.: Structural acoustics and vibrations. In: Springer Handbook of Acoustics, pp. 901–960. Springer, New York (2007)
9. Conklin, H.A.: Design and tone in the mechanoacoustic piano. Part III. Piano strings and scale design. J. Acoust. Soc. Am. **100**, 1286–1298 (1996)

10. Cummings, A.: Sound radiation from a plate into a porous medium. J. Sound Vib. **247**(3), 389–406 (2001)
11. Dérogis, P.: Analysis of the vibrations and radiation of an upright piano soundboard, and design of a system for reproducing its acoustic field (in French). Ph.D. thesis, Université du Maine, Le Mans (1997)
12. Elliott, S.J., Johnson, M.E.: Radiation modes and the active control of sound power. J. Acoust. Soc. Am. **94**(4), 2194–2204 (1993)
13. Gautier, F., Tahani, N.: Vibroacoustic behavior of a simplified musical wind instrument. J. Sound Vib. **213**(1), 107–125 (1998)
14. Gautier, F., Nief, G., Gilbert, J., Dalmont, J.: Vibro-acoustics of organ pipes-revisiting the Miller experiment. J. Acoust. Soc. Am. **131**, 737–738 (2012)
15. Gough, C.: Violin plate modes. J. Acoust. Soc. Am. **137**(1), 139–153 (2015)
16. Gough, C.E.: A violin shell model: vibrational modes and acoustics. J. Acoust. Soc. Am. **137**(3), 1210–1225 (2015)
17. Graff, K.F.: Wave Motion in Elastics Solids. Dover, New York (1991)
18. Griffin, S., Lane, S.A., Clark, R.L.: The application of smart structures towards feedback suppression in amplified acoustic guitars. J. Acoust. Soc. Am. **113**(6), 3188–3196 (2003)
19. Heckl, M.: Vibrations of one- and two- dimensional continuous systems. In: Encyclopaedia of Acoustics, vol. 2, pp. 735–752. Wiley, New York (1997)
20. Hu, Q., Wu, F.: An alternative formulation for predicting sound radiation from a vibrating object. J. Acoust. Soc. Am. **103**(4), 1763–1774 (1998)
21. Junger, M.C., Feit, D.: Sound, Structures and Their Interaction. Acoustical Society of America, Melville (1993)
22. Kausel, W., Chatziioannou, V., Moore, T., Gorman, B., Rokni, M.: Axial vibrations of brass wind instrument bells and their acoustical influence: theory and simulations. J. Acoust. Soc. Am. **137**, 3149–3162 (2015)
23. Lambourg, C., Chaigne, A.: Measurements and modeling of the admittance matrix at the bridge in guitars. In: Proceedings of the SMAC 93, pp. 448–453 (1993)
24. Le Pichon, A.: Method for predicting the acoustic radiation of volumic structures composed of one or several vibrating surfaces. Application to stringed musical instruments (in French). Ph.D. thesis, Université Paris 11 (1996)
25. Le Pichon, A., Berge, S., Chaigne, A.: Comparison between experimental and predicted radiation of a guitar. Acust. Acta Acust. **84**, 136–145 (1998)
26. Lesueur, C.: Acoustic radiation of structures (in French). Collection de la direction des études et recherches d'Electricité de France. Eyrolles, Paris (1988)
27. Nederveen, C.J., Dalmont, J.: Pitch and level changes in organ pipes due to wall resonances. J. Sound Vib. **27**, 227–239 (2004)
28. Nightingale, T.R.T., Bosmans, I.: On the drive-point mobility of a periodic rib-stiffened plate. Tech. Rep. NRCC-45609, National Research Council Canada, Ottawa (2006)
29. Pico, R.: Vibroacoustics of slightly bent cylindrical tubes. influence of the wall vibrations on the oscillations of wind musical instruments (in French). Ph.D. thesis, Universités du Maine (France) et de Valence (Espagne) (2004)
30. Quaegebeur, N.: Nonlinear vibrations and acoustic radiation of thin loudspeaker-like structures (in French). Ph.D. thesis, ENSTA ParisTech (2007)
31. Ruzzene, M.: Structural acoustics. Class notes, School of Aerospace Engineering, Georgia Institute of Technology (2003)
32. Schedin, S., Lambourg, C., Chaigne, A.: Transient sound fields from impacted plates: comparison between numerical simulations and experiments. J. Sound Vib. **221**(3), 471–490 (1999)
33. Skudrzyk, E.: The mean value method of predicting the dynamic response of complex vibrators. J. Acoust. Soc. Am. **67**(4), 1105–1135 (1980)
34. Soedel, W.: Vibrations of Shells and Plates, 3rd edn. Marcel Dekker, New York (2004)
35. Stepanishen, P.R.: Transient radiation from piston in an infinite baffle. J. Acoust. Soc. Am. **49**(5B), 1629–1638 (1971)

36. Suzuki, H.: Vibration and sound radiation of a piano soundboard. J. Acoust. Soc. Am. **80**(6), 1573–1582 (1986)
37. Suzuki, H., Tichy, J.: Diffraction of sound by a convex or a concave dome in an infinite baffle. J. Acoust. Soc. Am. **70**(5), 1480–1487 (1981)
38. Wallace, C.E.: Radiation resistance of a rectangular panel. J. Acoust. Soc. Am. **51**, 946–952 (1972)
39. Williams, E.G.: Numerical evaluation of the radiation from unbaffled finite plates using the FFT. J. Acoust. Soc. Am. **73**, 343–347 (1983)
40. Williams, E.G.: Fourier Acoustics: Sound Radiation and Nearfield Acoustical Holography. Academic, New York (1999)
41. Wolfe, J.: Music acoustics web page, the University of New South Wales. http://www.phys.unsw.edu.au/music/ (2007)